

1 High-level cognition during story listening is reflected in
2 high-order dynamic correlations in neural activity patterns

3 Lucy L. W. Owen¹, Thomas H. Chang^{1,2}, and Jeremy R. Manning^{1,†}

¹Department of Psychological and Brain Sciences,
Dartmouth College, Hanover, NH

²Amazon.com, Seattle, WA

†Address correspondence to jeremy.r.manning@dartmouth.edu

4 August 11, 2021

5 **Abstract**

6 Our thoughts arise from coordinated patterns of interactions between brain structures that change with
7 our ongoing experiences. High-order dynamic correlations in neural activity patterns reflect different sub-
8 graphs of the brain's functional connectome that display homologous lower-level dynamic correlations. We
9 tested Here we test the hypothesis that high-level cognition is reflected in high-order dynamic correlations
10 in brain activity patterns. We developed develop an approach to estimating high-order dynamic corre-
11 lations in timeseries data, and we applied apply the approach to neuroimaging data collected as human
12 participants either listened listen to a ten-minute story or listened listen to a temporally scrambled version
13 of the story. We trained train across-participant pattern classifiers to decode (in held-out data) when in
14 the session each neural activity snapshot was collected. We found find that classifiers trained to decode
15 from high-order dynamic correlations yielded yield the best performance on data collected as participants
16 listened to the (unscrambled) story. By contrast, classifiers trained to decode data from scrambled versions
17 of the story yielded the best performance when they were trained using first-order dynamic correlations
18 or non-correlational activity patterns. We suggest that as our thoughts become more complex, they are
19 reflected in higher-order patterns of dynamic network interactions throughout the brain.

20 **Introduction**

21 A central goal in cognitive neuroscience is to elucidate the neural code: neural code: i.e. the mapping between
22 (a) mental states or cognitive representations and (b) neural activity patterns. One means of testing models of
23 the neural code is to ask how accurately that model is able to "translate" neural activity patterns into known
24 (or hypothesized) mental states or cognitive representations (e.g., 1; 2; 3; 4; 5; 6; 7; 8; 9)(1; 2; 3; 4; 5; 6; 7; 8; 9)
25 . Training decoding models on different types of neural features (Fig. 1a) can also help to elucidate which
26 specific aspects of neural activity patterns are informative about cognition and, by extension, which types of
27 neural activity patterns might compose the neural code. For example, prior work has used region of interest
28 analyses to estimate the anatomical locations of specific neural representations (e.g., 10)(10), or to compare
29 the relative contributions to the neural code of multivariate activity patterns versus dynamic correlations
30 between neural activity patterns (e.g., 11; 12)(11; 12). An emerging theme in this literature is that cognition

31 is mediated by dynamic interactions between brain structures (13;14;15;16;17;18;19;20;21;22;23;24;25)
32 (13;14;15;16;17;18;19;20;21;22;23;24;25).

33 [Figure 1 about here.]

34 Studies of the neural code to date have primarily focused on univariate or multivariate neural pat-
35 terns (for review see 2)(2), or (more recently) on patterns of dynamic first-order correlations (i.e., interactions between pairs o
36 (i.e., interactions between pairs of brain structures (11;12;18;20;21;22)). What might the future of this line
37 of work hold? For example, is the neural code implemented through higher-order interactions between
38 brain structures (e.g., see 26)(26)? Second-order correlations reflect *homologous* homologous patterns of cor-
39 relation. In other words, if the dynamic patterns of correlations between two regions, *A* and *B*, are similar
40 to those between two other regions, *C* and *D*, this would be reflected in the second-order correlations be-
41 tween (*A*-*B*) and (*C*-*D*). In this way, second-order correlations identify similarities and differences between
42 subgraphs of the brain's connectome. Analogously, third-order correlations reflect homologies between
43 second-order correlations— i.e., homologous patterns of homologous interactions between brain regions.
44 More generally, higher-order correlations reflect homologies between patterns of lower-order correlations.
45 We can then ask: which “orders” of interaction are most reflective of high-level cognitive processes?

46 One reason one might expect to see homologous networks in a dataset is related to the notion that network
47 dynamics reflect ongoing neural computations or cognitive processing (e.g., 27)(27). If the nodes in two
48 brain networks are interacting (within each network) in similar ways then, according to our characterization
49 of network dynamics, we refer to the similarities between those patterns of interaction as higher-order
50 correlations. When higher-order correlations are themselves changing over time, we can also attempt to
51 capture and characterize those high-order dynamics.

52 Another central question pertains to the extent to which the neural code is carried by activity patterns that
53 directly reflect ongoing cognition (e.g., following 1;2)(1;2), versus the dynamic properties of the network
54 structure itself, independent of specific activity patterns in any given set of regions (e.g., following 16)
55 (16). For example, graph measures such as centrality and degree (28)(28) may be used to estimate how
56 a given brain structure is “communicating” with other structures, independently of the specific neural
57 representations carried by those structures. If one considers a brain region's position in the network (e.g.,
58 its eigenvector centrality) as a dynamic property, one can compare how the positions of different regions are
59 correlated, and/or how those patterns of correlations change over time. We can also compute higher-order
60 patterns in these correlations to characterize homologous subgraphs in the connectome that display similar
61 changes in their constituent brain structures' interactions with the rest of the brain.

62 To gain insights into the above aspects of the neural code, we developed a computational framework

for estimating dynamic high-order correlations in timeseries data. This framework provides an important advance, in that it enables us to examine patterns of higher-order correlations that are computationally intractable to estimate via conventional methods. Given a multivariate timeseries, our framework provides timepoint-by-timepoint estimates of the first-order correlations, second-order correlations, and so on. Our approach combines a kernel-based method for computing dynamic correlations in timeseries data with a dimensionality reduction step (Fig. 1b) that projects the resulting dynamic correlations into a low-dimensional space. We explored two dimensionality reduction approaches: principle components analysis (PCA; 29)(29)(PCA), which preserves an approximately invertible transformation back to the original data (e.g., ~~this follows related approaches taken by 30; 31; 32~~; (30; 31; 32), and a second non-invertible algorithm for computing dynamic patterns in eigenvector centrality (33)(33). This latter approach characterizes correlations between each feature dimension's relative *position* *position* in the network (at each moment in time) in favor of the specific activity histories of different features (also see 26; 34; 35)(26; 34; 35).

We validated our approach using synthetic data where the underlying correlations were known. We then applied our framework to a neuroimaging dataset collected as participants listened to either an audio recording of a ten-minute story, listened to a temporally scrambled version of the story, or underwent a resting state scan (36)(36). Temporal scrambling has been used in a growing number of studies, largely by Uri Hasson's group, to identify brain regions that are sensitive to higher-order and longer-timescale information (e.g., cross-sensory integration, rich narrative meaning, complex situations, etc.) versus regions that are primarily sensitive to low-order (e.g., sensory) information. For example, (37) argues that when brain areas are sensitive to fine versus coarse temporal scrambling, this indicates that they are "higher order" in the sense that they process contextual information pertaining to further-away timepoints. By contrast, low-level regions, such as primary sensory cortices, do not meaningfully change their responses (after correcting for presentation order) even when the stimulus is scrambled at fine timescales.

We used a subset of the story listening and rest data to train across-participant classifiers to decode listening times (of groups of participants) using a blend of neural features (comprising neural activity patterns, as well as different orders of dynamic correlations between those patterns that were inferred using our computational framework). We found that both the PCA-based and eigenvector centrality-based approaches yielded neural patterns that could be used to decode accurately (i.e., well above chance). Both approaches also yielded the best decoding accuracy for data collected during (intact) story listening when high-order (PCA: second-order; eigenvector centrality: fourth-order) dynamic correlation patterns were included as features. When we trained classifiers on the scrambled stories or resting state data, only (relatively) lower-order dynamic patterns were informative to the decoders. Taken together, our results indicate that high-level cognition is supported by high-order dynamic patterns of communication between

96 brain structures.

97 Results

98 We sought to understand whether high-level cognition is reflected in dynamic patterns of high-order cor-
99 relations. To that end, we developed a computational framework for estimating the dynamics of stimulus-
100 driven high-order correlations in multivariate timeseries data (see *Dynamic inter-subject functional connectivity*
(DISFC) and *Dynamic higher-order correlations**Dynamic inter-subject functional connectivity (DISFC) and*
Dynamic higher-order correlations). We evaluated the efficacy of this framework at recovering known pat-
101 terns in several synthetic datasets (see *Synthetic data: simulating dynamic first-order correlations* and *Synthetic*
*data: simulating dynamic higher-order correlations**Synthetic data: simulating dynamic first-order correlations*
and Synthetic data: simulating dynamic higher-order correlations). We then applied the framework to a
102 public fMRI dataset collected as participants listened to an auditorily presented story, listened to a tem-
103 porally scrambled version of the story, or underwent a resting state scan (see *Functional neuroimaging data*
*collected during story listening**Functional neuroimaging data collected during story listening*). We used the
104 relative decoding accuracies of classifiers trained on different sets of neural features to estimate which types
105 of features reflected ongoing cognitive processing.
106

111 Recovering known dynamic *first-order* correlations*from synthetic data*

112 *Recovering dynamic first-order correlations*

113 We generated synthetic datasets that differed in how the underlying first-order correlations changed over
114 time. For each dataset, we applied Equation 4 with a variety of kernel shapes and widths. We assessed how
115 well the true underlying correlations at each timepoint matched the recovered correlations (Fig. 2). For every
116 kernel and dataset we tested, our approach recovered the correlation dynamics we embedded into the data.
117 However, the quality of these recoveries varied across different synthetic datasets in a kernel-dependent
118 way.

119 [Figure 2 about here.]

120 In general, wide monotonic kernel shapes (Laplace, Gaussian), and wider kernels (within a shape),
121 performed best when the correlations varied gradually from moment-to-moment (Figs. 2a, c, and d). In the
122 extreme, as the rate of change in correlations approaches 0 (Fig. 2a), an infinitely wide kernel would exactly
123 recover the Pearson's correlation (e.g., compare Eqns. 1 and 4).

124 When the correlation dynamics were unstructured in time (Fig. 2b), a Dirac δ kernel (infinitely nar-
125 row) performed best. This is because, when every timepoint's correlations are independent ~~from~~~~of~~ the
126 correlations at every other timepoint, averaging data over time dilutes the available signal. Following a
127 similar pattern, holding kernel shape fixed, narrower kernel parameters better recovered randomly varying
128 correlations.

129 **Recovering dynamic higher-order correlations**

130 **Recovering known dynamic higher-order correlations**

131 Following our approach to evaluating our ability to recover known dynamic first-order correlations from
132 synthetic data, we generated an analogous second set of synthetic datasets that we designed to exhibit known
133 dynamic first-order ~~and~~ and second-order correlations (see *Synthetic data: simulating dynamic higher-order*
134 *correlations*~~Synthetic data: simulating dynamic higher-order correlations~~). We generated a total of 400
135 datasets ~~(100 datasets for each category)~~ that varied in how the first-order and second-order correlations
136 changed over time. We then repeatedly applied Equation 4 using the overall best-performing kernel from
137 our first-order tests (a Laplace kernel with a width of 20; Fig. 2) to assess how closely the recovered dynamic
138 correlations matched the dynamic correlations we had embedded into the datasets.

139 Overall, we found that we could reliably recover both first-order and second-order correlations from
140 the synthetic data (Fig. 3). When the correlations were stable for longer intervals, or changed gradually
141 (constant, ramping, and event datasets), recovery performance was relatively high, and we were better
142 able to recover dynamic first-order correlations than second-order correlations. This is because errors in
143 our ~~estimation~~ estimation procedure at lower orders necessarily propagate to higher orders (since lower-
144 order correlations are used to estimate higher-order correlations). Conversely, when the correlations were
145 particularly ~~unstable~~ unstable (random datasets), we better recovered second-order correlations. This is
146 because noise in our ~~data generation~~ data generation procedure propagates from higher orders to lower
147 orders (see *Synthetic data: simulating dynamic high-order correlations*~~Synthetic data: simulating dynamic~~
148 high-order correlations).

149 [Figure 3 about here.]

150 We also examined the impact of the data duration (Fig. S3) and complexity (number of zero-order features;
151 Fig. S4) on our ability to accurately recover ground truth first-order and second-order dynamic correlations.
152 In general, we found that our approach better recovers ground truth dynamic correlations from longer
153 duration timeseries data. We also found that our approach tends to best recover data generated using fewer

154 zero-order features (i.e., lower complexity), although this tendency was not strictly monotonic. Further,
155 because our data generation procedure requires $O(K^4)$ memory to generate a second-order timeseries with K
156 zero-order features, we were not able to fully explore how the number of zero-order features affects recovery
157 accuracy as the number of features gets larger (e.g., as it approaches the number of features present in the
158 fMRI data we examine below). Although we were not able to formally test this to our satisfaction, we expect
159 that accurately estimating dynamic high-order correlations would require data with many more zero-order
160 features than we were able to simulate. Our reasoning is that high-order correlations necessarily involve
161 larger numbers of lower-order features, so achieving adequate “resolution” high-order timeseries might
162 require many low-order features.

163 Taken together, our explorations using synthetic data indicated that we are able to partially, but not
164 perfectly, recover ground truth dynamic first-order and second-order correlations. This suggests that our
165 modeling approach provides a meaningful (if noisy) estimate of high-order correlations. We next turned
166 to analyses of human fMRI data to examine whether the recovered dynamics might reflect the dynamics of
167 human cognition during a naturalistic story-listening task.

168 Cognitively relevant dynamic high-order correlations in fMRI data

169 We used across-participant temporal decoders to identify cognitively relevant neural patterns in fMRI
170 data (see *Forward inference and decoding accuracy*[Forward inference and decoding accuracy](#)). The dataset
171 we examined ([collected by 36](#))[\(36\)](#) comprised four experimental conditions that exposed participants to
172 stimuli that varied systematically in how cognitively engaging they were. The *intact experimental condition*
173 [intact experimental condition \(intact\)](#) had participants listen to an audio recording of a 10-minute story. The
174 *paragraph-scrambled experimental condition*[paragraph-scrambled experimental condition \(paragraph\)](#) had
175 participants listen to a temporally scrambled version of the story, where the paragraphs occurred out of order
176 (but where the same total set of paragraphs were presented over the full listening interval). All participants
177 in this condition experienced the scrambled paragraphs in the same order. The *word-scrambled experimental*
178 [condition word-scrambled experimental condition \(word\)](#) had participants listen to a temporally scrambled
179 version of the story where the words in the story occurred in a random order. All participants in the word
180 condition experienced the scrambled words in the same order. Finally, in a *rest experimental condition*
181 [rest experimental condition \(rest\)](#), participants lay in the scanner with no overt stimulus, with their eyes
182 open (blinking as needed). This public dataset provided a convenient means of testing our hypothesis that
183 different levels of cognitive processing and engagement are reflected in different orders of brain activity
184 dynamics.

185

[Figure 4 about here.]

186 In brief, we computed timeseries of dynamic high-order correlations that were similar across participants
 187 in each of two randomly assigned groups: a training group and a test group. We then trained classifiers
 188 on the training group's data to match each sample from the test group with a stimulus timepoint. Each
 189 classifier comprised a weighted blend of neural patterns that reflected up to n^{th} -order dynamic correlations
 190 (see *Feature weighting and testing*, Fig. 10*Feature weighting and testing*). We repeated this process for
 191 $n \in \{0, 1, 2, \dots, 10\}$. Our examinations of synthetic data suggested that none of the kernels we examined
 192 were "universal" in the sense of optimally recovering underlying correlations regardless of the temporal
 193 structure of those correlations. We found a similar pattern in the (real) fMRI data, whereby different kernels
 194 yielded different decoding accuracies, but no single kernel emerged as the clear "best." In our analyses
 195 of neural data, we therefore averaged our decoding results over a variety of kernel shapes and widths
 196 in order to identify results that were robust to specific kernel parameters (see *Identifying robust decoding*
 197 *results**Identifying robust decoding results*).

198 Our approach to estimating dynamic high-order correlations entails mapping the high-dimensional
 199 feature space of correlations (represented by a T by $O(K^2)$ matrix) onto a lower-dimensional feature space
 200 (represented by a T by K matrix). We carried out two sets of analyses that differed in how this mapping was
 201 computed. The first set of analyses used PCA to find a low-dimensional embedding of the original dynamic
 202 correlation matrices (Fig. 4a,b). The second set of analyses characterized correlations in dynamics of each
 203 feature's eigenvector centrality, but did not preserve the underlying activity dynamics (Fig. 4c,d).

204

[Figure 5 about here.]

205 Both sets of temporal decoding analyses yielded qualitatively similar results for the auditory (non-rest)
 206 conditions of the experiment (Fig. 4: pink, green, and teal lines; Fig. 5: three leftmost columns). The highest
 207 decoding accuracy for participants who listened to the intact (unscrambled) story was achieved using high-
 208 order dynamic correlations (PCA: second-order; eigenvector-centrality: fourth-order). Scrambled versions
 209 of the story were best decoded by lower-order correlations (PCA/paragraph: first-order; PCA/word: order
 210 zero; eigenvector centrality/paragraph: order zero; eigenvector centrality/word: order zero). The two sets
 211 of analyses yielded different decoding results on resting state data (Fig. 4: purple lines; Fig. 5: rightmost
 212 column). We note that, while the resting state times could be decoded reliably, the accuracies were only very
 213 slightly above chance. We speculate that the decoders might have picked up on attentional drift, boredom,
 214 or tiredness; we hypothesize that these all increased throughout the resting state scan. The decoders might
 215 be picking up on aspects of these loosely defined cognitive states that are common across individuals. The

216 PCA-based approach achieved the highest resting state decoding accuracy using order zero features (non-
217 correlational, activation-based), whereas the eigenvector centrality-based approach achieved the highest
218 resting state decoding accuracy using second-order correlations. Taken together, these analyses indicate
219 that high-level cognitive processing (while listening to the intact story) is reflected in the dynamics of high-
220 order correlations in brain activity, whereas lower-level cognitive processing (while listening to scrambled
221 versions of the story that lack rich meaning) is reflected in the dynamics of lower-order correlations and
222 non-correlational activity dynamics. Further, these patterns are associated both with the underlying activity
223 patterns (characterized using PCA) and also with the changing relative positions that different brain areas
224 occupy in their associated networks (characterized using eigenvector centrality).

225 [Figure 6 about here.]

226 Having established that patterns of high-order correlations are informative to decoders, we next won-
227 dered which specific networks of brain regions contributed most to these patterns. As a representative
228 example, we selected the kernel parameters that yielded decoding accuracies that were the most strongly
229 correlated (across conditions and orders) with the average accuracies across all of the kernel parameters
230 we examined. Using Figure 4c as a template, the best-matching kernel was a Laplace kernel with a width
231 of 50 (Fig. 9d; also see Fig. S9). We used this kernel to compute a single K by K n^{th} -order DISFC matrix
232 for each experimental condition. We then used Neurosynth (38)(38) to compute the terms most highly
233 associated with the most strongly correlated pairs of regions in each of these matrices (Fig. 6; see *Reverse*
234 *inference*Reverse inference).

235 For all of the story listening conditions (intact, paragraph, and word; top three rows of Fig. 6), we
236 found that first- and second-order correlations were most strongly associated with auditory and speech
237 processing areas. During intact story listening, third-order correlations reflected integration with visual
238 areas, and fourth-order correlations reflected integration with areas associated with high-level cognition
239 and cognitive control, such as the ventrolateral prefrontal cortex. However, when participants listened to
240 temporally scrambled stories, these higher-order correlations instead involved interactions with additional
241 regions associated with speech and semantic processing (second and third rows of Fig. 6). By contrast, we
242 found a much different set of patterns in the resting state data (Fig. 6, bottom row). First-order resting state
243 correlations were most strongly associated with regions involved in counting and numerical understand-
244 ing. Second-order resting state correlations were strongest in visual areas; third-order correlations were
245 strongest in task-positive areas; and fourth-order correlations were strongest in regions associated with
246 autobiographical and episodic memory. We carried out analogous analyses to create maps (and decode
247 the top associated Neurosynth terms) for up to fifteenth-order correlations (Figs. S5, S6, S7, and S8). Of

248 note, examining fifteenth-order correlations between 700 nodes using conventional methods would have
249 required storing roughly $\frac{700^{2 \times 15}}{2} \approx 1.13 \times 10^{85}$ floating point numbers—assuming single-precision (32 bits
250 each), this would require roughly 32 times as many bits as there are molecules in the known universe!
251 Although these fifteenth-order correlations do appear (visually) to have some well-formed structure, we
252 provide this latter example primarily as a demonstration of the efficiency and scalability of our approach.

253 Discussion

254 We tested the hypothesis that high-level cognition is reflected in high-order brain network dynamics (e.g., see 19; 26)
255 (19; 26). We examined high-order network dynamics in functional neuroimaging data collected during a
256 story listening experiment. When participants listened to an auditory recording of the story, participants
257 exhibited similar high-order brain network dynamics. By contrast, when participants instead listened to
258 temporally scrambled recordings of the story, only lower-order brain network dynamics were similar across
259 participants. Our results indicate that higher orders of network interactions support higher-level aspects of
260 cognitive processing (Fig. 7).

261 [Figure 7 about here.]

262 The notion that cognition is reflected in (and possibly mediated by) patterns of first-order network dy-
263 namics has been suggested by or proposed in myriad empirical studies and reviews (e.g., 11; 12; 17; 18; 20; 21; 22; 24; 25; 32; 39;
264 (11; 12; 17; 18; 20; 21; 22; 24; 25; 32; 39; 40; 41; 42). Our study extends this line of work by finding cognitively
265 relevant *higher-order* *higher-order* network dynamics that reflect ongoing cognition. Our findings also com-
266 plement other work that uses graph theory and topology to characterize how brain networks reconfigure
267 during cognition (e.g., 16; 26; 30; 31; 34; 35; 43)(16; 26; 30; 31; 34; 35; 43).

268 An open question not addressed by our study pertains to how different structures integrate incoming
269 information with different time constants. For example, one line of work suggests that the cortical surface
270 comprises a structured map such that nearby brain structures process incoming information at similar
271 timescales. Low-level sensory areas integrate information relatively quickly, whereas higher-level regions
272 integrate information relatively slowly (37; 44; 45; 46; 47; 48; 49)(37; 44; 45; 46; 47; 48; 49). A similar hierar-
273 chy appears to play a role in predicting future events (50)(50). Other related work in human and mouse
274 brains indicates that the temporal response profile of a given brain structure may relate to how strongly
275 connected that structure is with other brain areas (51)(51). Further study is needed to understand the role
276 of temporal integration at different scales of network interaction, and across different anatomical structures.
277 Importantly, our analyses do not speak to the physiological basis of higher-order dynamics, and could

reflect nonlinearities, chaotic patterns, non-stationarities, and/or multistability, etc. However, our decoding analyses do indicate that higher-order dynamics are consistent across individuals, and therefore unlikely to reflect non-stimulus-driven dynamics that are unlikely to be similar across individuals.

One limitation of our approach relates to how noise propagates in our estimation procedure. Specifically, our procedure for estimating high-order dynamic correlations depends on estimates of lower-order dynamic correlations. This means that our measures of which higher-order patterns are reliable and stable across experimental conditions are partially confounded with the stability of lower-order patterns. Prior work suggests that the stability of what we refer to here as first-order dynamics likely varies across the experimental conditions we examined (36)(36). Therefore a caveat to our claim that richer stimuli evoke more stable higher-order dynamics is that our approach assumes that those high-order dynamics reflect relations or interactions between lower-order features.

Another potential limitation of our approach relates to recent work suggesting that the brain undergoes rapid state changes, for example across event boundaries (e.g., 44)(44). (52) used hidden semi-Markov models to estimate state-specific network dynamics (also see 53)(53). Our general approach might be extended by considering putative state transitions. For example, rather than weighting all timepoints using a similar kernel (Eqn. 4), the kernel function could adapt on a timepoint-by-timepoint basis such that only timepoints determined to be in the same “state” were given non-zero weight.

Identifying high-order network dynamics associated with high-level cognition required several important methods advances. First, we used kernel-based dynamic correlations to extended the notion of (static) inter-subject functional connectivity (36)(36) to a dynamic measure of inter-subject functional connectivity (DISFC) that does not rely on sliding windows (e.g., as in 11)(11), and that may be computed at individual timepoints. This allowed us to precisely characterize stimulus-evoked network dynamics that were similar across individuals. Second, we developed a computational framework for efficiently and scalably estimating high-order dynamic correlations. Our approach uses dimensionality reduction algorithms and graph measures to obtain low-dimensional embeddings of patterns of network dynamics. Third, we developed an analysis framework for identifying robust decoding results by carrying out our analyses using a range of parameter values and identifying which results were robust to specific parameter choices. By showing that high-level cognition is reflected in high-order network dynamics, we have elucidated the next step on the path towards understanding the neural basis of cognition.

307 **Methods**

308 Our general approach to efficiently estimating high-order dynamic correlations comprises four general
309 steps (Fig. 8). First, we derive a kernel-based approach to computing dynamic pairwise correlations in
310 a T (timepoints) by K (features) multivariate timeseries, \mathbf{X}_0 . This yields a T by $O(K^2)$ matrix of dynamic
311 correlations, \mathbf{Y}_1 , where each row comprises the upper triangle and diagonal of the correlation matrix at
312 a single timepoint, reshaped into a row vector (this reshaped vector is $(\frac{K^2-K}{2} + K)$ -dimensional). Second,
313 we apply a dimensionality reduction step to project the matrix of dynamic correlations back onto a K -
314 dimensional space. This yields a T by K matrix, \mathbf{X}_1 , that reflects an approximation of the dynamic correlations
315 reflected in the original data. Third, we use repeated applications of the kernel-based dynamic correlation
316 step to \mathbf{X}_n and the dimensionality reduction step to the resulting \mathbf{Y}_{n+1} to estimate high-order dynamic
317 correlations. Each application of these steps to a T by K time series \mathbf{X}_n yields a T by K matrix, \mathbf{X}_{n+1} , that
318 reflects the dynamic correlations between the columns of \mathbf{X}_n . In this way, we refer to n as the *order* order of the
319 timeseries, where \mathbf{X}_0 (order 0) denotes the original data and \mathbf{X}_n denotes (approximated) n^{th} -order dynamic
320 correlations between the columns of \mathbf{X}_0 . Finally, we use a cross-validation-based decoding approach to
321 evaluate how well information contained in a given order (or weighted mixture of orders) may be used
322 to decode relevant cognitive states. If including a given \mathbf{X}_n in the feature set yields higher classification
323 accuracy on held-out data, we interpret this as evidence that the given cognitive states are reflected in
324 patterns of n^{th} -order correlations.

325 All of the code used to produce the figures and results in this manuscript, along with links to the
326 corresponding datasets, may be found at github.com/ContextLab/timecorr-paper. In addition, we have
327 released a Python toolbox for computing dynamic high-order correlations in timeseries data; our toolbox
328 may be found at timecorr.readthedocs.io.

329 [Figure 8 about here.]

330 **Kernel-based approach for computing dynamic correlations**

Given a T by K matrix of observations, \mathbf{X} , we can compute the (static) Pearson's correlation between any pair of columns, $\mathbf{X}(\cdot, i)$ and $\mathbf{X}(\cdot, j)$ using (29)(29):

$$\text{corr}(\mathbf{X}(\cdot, i), \mathbf{X}(\cdot, j)) = \frac{\sum_{t=1}^T (\mathbf{X}(t, i) - \bar{\mathbf{X}}(\cdot, i))(\mathbf{X}(t, j) - \bar{\mathbf{X}}(\cdot, j))}{\sqrt{\sum_{t=1}^T \sigma_{\mathbf{X}(\cdot, i)}^2 \sigma_{\mathbf{X}(\cdot, j)}^2}}, \text{ where} \quad (1)$$

$$\bar{\mathbf{X}}(\cdot, k) = \frac{1}{T} \sum_{t=1}^T \mathbf{X}(t, k), \text{ and} \quad (2)$$

$$\sigma_{\mathbf{X}(\cdot, k)}^2 = \frac{1}{T} \sum_{t=1}^T (\mathbf{X}(t, k) - \bar{\mathbf{X}}(\cdot, k))^2 \quad (3)$$

- 331 We can generalize this formula to compute time-varying correlations by incorporating a *kernel function* *kernel*
- 332 *function* that takes a time t as input, and returns how much the observed data at each timepoint $\tau \in [-\infty, \infty]$
- 333 contributes to the estimated instantaneous correlation (54) at time t (Fig. 9; also see 54, for a similar approach)
- 334 (Fig. 9).

335 [Figure 9 about here.]

Given a kernel function $\kappa_t(\cdot)$ for timepoint t , evaluated at timepoints $\tau \in [1, \dots, T]$, we can update the static correlation formula in Equation 1 to estimate the *instantaneous correlation* *instantaneous correlation* at timepoint t :

$$\text{timecorr}_{\kappa_t}(\mathbf{X}(\cdot, i), \mathbf{X}(\cdot, j)) = \frac{\sum_{\tau=1}^T (\mathbf{X}(\tau, i) - \tilde{\mathbf{X}}_{\kappa_t}(\cdot, i))(\mathbf{X}(\tau, j) - \tilde{\mathbf{X}}_{\kappa_t}(\cdot, j))}{\sqrt{\sum_{\tau=1}^T \tilde{\sigma}_{\kappa_t}^2(\mathbf{X}(\cdot, i)) \tilde{\sigma}_{\kappa_t}^2(\mathbf{X}(\cdot, j))}}, \text{ where} \quad (4)$$

$$\tilde{\mathbf{X}}_{\kappa_t}(\cdot, k) = \sum_{\tau=1}^T \kappa_t(\tau) \mathbf{X}(\tau, k), \quad (5)$$

$$\tilde{\sigma}_{\kappa_t}^2(\mathbf{X}(\cdot, k)) = \sum_{\tau=1}^T (\mathbf{X}(\tau, k) - \tilde{\mathbf{X}}_{\kappa_t}(\cdot, k))^2. \quad (6)$$

- 336 Here $\text{timecorr}_{\kappa_t}(\mathbf{X}(\cdot, i), \mathbf{X}(\cdot, j))$ reflects the correlation at time t between columns i and j of \mathbf{X} , estimated using
- 337 the kernel κ_t . We evaluate Equation 4 in turn for each pair of columns in \mathbf{X} and for kernels centered on each
- 338 timepoint in the timeseries, respectively, to obtain a T by K by K timeseries of dynamic correlations, \mathbf{Y} . For
- 339 convenience, we then reshape the upper triangles and diagonals of each timepoint's symmetric correlation
- 340 matrix into a row vector to obtain an equivalent T by $(\frac{K^2-K}{2} + K)$ matrix.

³⁴¹ **Dynamic inter-subject functional connectivity (DISFC)**

Equation 4 provides a means of taking a single observation matrix, \mathbf{X}_n and estimating the dynamic correlations from moment to moment, \mathbf{Y}_{n+1} . Suppose that one has access to a set of multiple observation matrices that reflect the same phenomenon. For example, one might collect neuroimaging data from several experimental participants, as each participant performs the same task (or sequence of tasks). Let $\mathbf{X}_n^1, \mathbf{X}_n^2, \dots, \mathbf{X}_n^P$ reflect the T by K observation matrices ($n = 0$) or reduced correlation matrices ($n > 0$) for each of P participants in an experiment. We can use *inter-subject functional connectivity (ISFC; 36; 55)* *inter-subject functional connectivity (36; 55) (ISFC)* to compute the stimulus-driven correlations reflected in the multi-participant dataset at a given timepoint t using:

$$\bar{\mathbf{C}}(t) = M \left(R \left(\frac{1}{2P} \sum_{p=1}^P Z(\mathbf{Y}_{n+1}^p(t))^\top + Z(\mathbf{Y}_{n+1}^p(t)) \right) \right), \quad (7)$$

where M extracts and vectorizes the upper triangle and diagonal of a symmetric matrix, Z is the Fisher z-transformation (56)(56):

$$Z(r) = \frac{\log(1+r) - \log(1-r)}{2}, \quad (8)$$

R is the inverse of Z :

$$R(z) = \frac{\exp(2z-1)}{\exp(2z+1)}, \quad (9)$$

and $\mathbf{Y}_{n+1}^p(t)$ denotes the correlation matrix at timepoint t (Eqn. 4) between each column of \mathbf{X}_n^p and each column of the average \mathbf{X}_n from all *other other* participants, $\bar{\mathbf{X}}_n^p$:

$$\bar{\mathbf{X}}_n^p = \frac{1}{P-1} \sum_{q \in \setminus p} \mathbf{X}_n^q, \quad (10)$$

³⁴² where $\setminus p$ denotes the set of all participants other than participant p . In this way, the T by $(\frac{K^2-K}{2} + K)$ DISFC
³⁴³ matrix $\bar{\mathbf{C}}$ provides a time-varying extension of the ISFC approach developed by (36).

³⁴⁴ **Low-dimensional representations of dynamic correlations**

³⁴⁵ Given a T by $(\frac{K^2-K}{2} + K)$ matrix of n^{th} -order dynamic correlations, \mathbf{Y}_n , we propose two general approaches
³⁴⁶ to computing a T by K low-dimensional representation of those correlations, \mathbf{X}_n . The first approach uses
³⁴⁷ dimensionality reduction algorithms to project \mathbf{Y}_n onto a K -dimensional space. The second approach uses

348 graph measures to characterize the relative positions of each feature ($k \in [1, \dots, K]$) in the network defined
349 by the correlation matrix at each timepoint.

350 **Dimensionality reduction-based approaches to computing \mathbf{X}_n**

351 The modern toolkit of dimensionality reduction algorithms include Principal Components Analysis (PCA; 29)
352 (29) (PCA), Probabilistic PCA (PPCA; 57)(57) (PPCA), Exploratory Factor Analysis (EFA; 58)(58) (EFA), In-
353 dependent Components Analysis (ICA; 59; 60)(59; 60) (ICA), t -Stochastic Neighbor Embedding (t -SNE; 61)
354 (61) (t -SNE), Uniform Manifold Approximation and Projection (UMAP; 62)(62) (UMAP), non-negative ma-
355 trix factorization (NMF; 63)(63) (NMF), Topographic Factor Analysis (TFA; 64)(64) (TFA), Hierarchical Topo-
356 graphic Factor analysis (HTFA; 11)(11) (HTFA), Topographic Latent Source Analysis (TLSA; 65)(65) (TLSA),
357 dictionary learning (66; 67)(66; 67), and deep auto-encoders (68)(68), among others. While complete charac-
358 terizations of each of these algorithms is beyond the scope of the present manuscript, the general intuition
359 driving these approaches is to compute the T by K matrix, \mathbf{X} , that is closest to the original T by J matrix,
360 \mathbf{Y} , where (typically) $K \ll J$. The different approaches place different constraints on what properties \mathbf{X} must
361 satisfy and which aspects of the data are compared (and how) in order to optimize how well \mathbf{X} approximates
362 \mathbf{Y} .

363 Applying dimensionality reduction algorithms to \mathbf{Y} yields an \mathbf{X} whose columns reflect weighted combi-
364 nations (or nonlinear transformations) of the original columns of \mathbf{Y} . This has two main consequences. First,
365 with each repeated dimensionality reduction, the resulting \mathbf{X}_n has lower and lower fidelity (with respect to
366 what the “true” \mathbf{Y}_n might have looked like without using dimensionality reduction to maintain tractability).
367 In other words, computing \mathbf{X}_n is a lossy operation. Second, whereas each column of \mathbf{Y}_n may be mapped
368 directly onto specific pairs of columns of \mathbf{X}_{n-1} , the columns of \mathbf{X}_n reflect weighted combinations and/or
369 nonlinear transformations of the columns of \mathbf{Y}_n . Many dimensionality reduction algorithms are invertible
370 (or approximately invertible). However, attempting to map a given \mathbf{X}_n back onto the original feature space
371 of \mathbf{X}_0 will usually require $O(TK^2)$ space and therefore becomes intractable as n or K grow large.

372 **Graph measure approaches to computing \mathbf{X}_n**

373 The above dimensionality reduction approaches to approximating a given \mathbf{Y}_n with a lower-dimensional
374 \mathbf{X}_n preserve a (potentially recombined and transformed) mapping back to the original data in \mathbf{X}_0 . We also
375 explore graph measures that instead characterize each feature’s relative *position* position in the broader
376 network of interactions and connections. To illustrate the distinction between the two general approaches
377 we explore, suppose a network comprises nodes A and B , along with several other nodes. If A and B exhibit

378 uncorrelated activity patterns, then by definition the functional connection (correlation) between them will
379 be close to 0. However, if A and B each interact with *other other* nodes in similar ways, we might attempt
380 to capture those similarities between A 's and B 's interactions with those other members of the network.

381 In general, graph measures take as input a matrix of interactions (e.g., using the above notation, a K
382 by K correlation matrix or binarized correlation matrix reconstituted from a single timepoint's row of \mathbf{Y}),
383 and return as output a set of K measures describing how each node (feature) sits within that correlation
384 matrix with respect to the rest of the population. Widely used measures include betweenness centrality
385 (the proportion of shortest paths between each pair of nodes in the population that involves the given node in question; e.g.,
386 (the proportion of shortest paths between each pair of nodes in the population that involves the given node in
387 question (69; 70; 71; 72; 73)); diversity and dissimilarity (characterizations of how differently connected a given node is from
388 (characterizations of how differently connected a given node is from others in the population (74; 75; 76));
389 eigenvector centrality and pagerank centrality (measures of how influential a given node is within the broader network; e.g.,
390 (measures of how influential a given node is within the broader network (77; 78; 79; 80)); transfer entropy and
391 flow coefficients (a measure of how much information is flowing from a given node to other nodes in the network; e.g., 81;
392 (a measure of how much information is flowing from a given node to other nodes in the network (81; 82)); k -
393 coreness centrality (a measure of the connectivity of a node within its local subgraph; e.g., 83; 84)(a measure
394 of the connectivity of a node within its local subgraph (83; 84)); within-module degree (a measure of how many connections a
395 (a measure of how many connections a node has to its close neighbors in the network (85)); participation co-
396 efficient (a measure of the diversity of a node's connections to different subgraphs in the network; e.g., 85)
397 (a measure of the diversity of a node's connections to different subgraphs in the network (85)); and sub-
398 graph centrality (a measure of a node's participation in all of the network's subgraphs; e.g., 86)(a measure
399 of a node's participation in all of the network's subgraphs (86)); among others.

400 For a given graph measure, $\eta : \mathbb{R}^{K \times K} \rightarrow \mathbb{R}^K$, we can use η to transform each row of \mathbf{Y}_n in a way that
401 characterizes the corresponding graph properties of each column. This results in a new T by K matrix,
402 \mathbf{X}_n , that reflects how the features reflected in the columns of \mathbf{X}_{n-1} participate in the network during each
403 timepoint (row).

404 Dynamic higher-order correlations

405 Because \mathbf{X}_n has the same shape as the original data \mathbf{X}_0 , approximating \mathbf{Y}_n with a lower-dimensional \mathbf{X}_n
406 enables us to estimate high-order dynamic correlations in a scalable way. Given a T by K input matrix, the
407 output of Equation 4 requires $O(TK^2)$ space to store. Repeated applications of Equation 4 (i.e., computing
408 dynamic correlations between the columns of the outputted dynamic correlation matrix) each require

409 exponentially more space; in general the n^{th} -order dynamic correlations of a T by K timeseries occupies
410 $O(TK^{2^n})$ space. However, when we approximate or summarize the output of Equation 4 with a T by K matrix
411 (as described above), it becomes feasible to compute even very high-order correlations in high-dimensional
412 data. Specifically, approximating the n^{th} -order dynamic correlations of a T by K timeseries requires only
413 $O(TK^2)$ additional space— the same as would be required to compute first-order dynamic correlations. In
414 other words, the space required to store $n + 1$ multivariate timeseries reflecting up to n^{th} order correlations
415 in the original data scales linearly with n using our approach (Fig. 8).

416 Data

417 We examined two types of data: synthetic data and human functional neuroimaging data. We constructed
418 and leveraged the synthetic data to evaluate our general approach (for a related validation approach see 87)
419 (87). Specifically, we tested how well Equation 4 could be used to recover known dynamic correlations using
420 different choices of kernel (κ ; Fig. 9), for each of several synthetic datasets that exhibited different temporal
421 properties. We also simulated higher-order correlations and tested how well Equation 4 could recover these
422 correlations using the best kernel from the previous synthetic data analyses. We then applied our approach
423 to a functional neuroimaging dataset to test the hypothesis that ongoing cognitive processing is reflected
424 in high-order dynamic correlations. We used an across-participant classification test to estimate whether
425 dynamic correlations of different orders contain information about which timepoint in a story participants
426 were listening to.

427 Synthetic data: simulating dynamic first-order correlations

428 We constructed a total of 400 different multivariate timeseries, collectively reflecting a total of 4 qualitatively
429 different patterns of dynamic first-order correlations (i.e., 100 datasets reflecting each type of dynamic pat-
430 tern). Each timeseries comprised 50 features (dimensions) that varied over 300 timepoints. The observations
431 at each timepoint were drawn from a zero-mean multivariate Gaussian distribution with a covariance matrix
432 defined for each timepoint as described below. We drew the observations at each timepoint independently
433 from the draws at all other timepoints; in other words, for each observation $s_t \sim \mathcal{N}(\mathbf{0}, \Sigma_t)$ at timepoint t ,
434 $p(s_t) = p(s_t | s_{\setminus t})$.

Constant. We generated data with stable underlying correlations to evaluate how Equation 4 characterized correlation “dynamics” when the ground truth correlations were static. We constructed 100 multivariate timeseries whose observations were each drawn from a single (stable) Gaussian distribution. For each

dataset (indexed by m), we constructed a random covariance matrix, Σ_m :

$$\Sigma_m = \mathbf{C}\mathbf{C}^\top, \text{ where} \quad (11)$$

$$\mathbf{C}(i, j) \sim \mathcal{N}(0, 1), \text{ and where} \quad (12)$$

435 $i, j \in [1, 2, \dots, 50]$. In other words, all of the observations (for each of the 300 timepoints) within each dataset
436 were drawn from a multivariate Gaussian distribution with the same covariance matrix, and the 100 datasets
437 each used a different covariance matrix.

438 **Random.** We generated a second set of 100 synthetic datasets whose observations at each timepoint were
439 drawn from a Gaussian distribution with a new randomly constructed (using Eqn. 11) covariance matrix.
440 Because each timepoint's covariance matrix was drawn independently from the covariance matrices for all
441 other timepoints, these datasets provided a test of reconstruction accuracy in the absence of any meaningful
442 underlying temporal structure in the dynamic correlations underlying the data.

Ramping. We generated a third set of 100 synthetic datasets whose underlying correlations changed gradually over time. For each dataset, we constructed two *anchor* *"anchor"* covariance matrices using Equation 11, Σ_{start} and Σ_{end} . For each of the 300 timepoints in each dataset, we drew the observations from a multivariate Gaussian distribution whose covariance matrix at each timepoint $t \in [0, \dots, 299]$ was given by

$$\Sigma_t = \left(1 - \frac{t}{299}\right)\Sigma_{\text{start}} + \frac{t}{299}\Sigma_{\text{end}}. \quad (13)$$

443 The gradually changing correlations underlying these datasets allow us to evaluate the recovery of dynamic
444 correlations when each timepoint's correlation matrix is unique (as in the random datasets), but where the
445 correlation dynamics are structured and exhibit first-order autocorrelations (as in the constant datasets).

446 **Event.** We generated a fourth set of 100 synthetic datasets whose underlying correlation matrices exhibited
447 prolonged intervals of stability, interspersed with abrupt changes. For each dataset, we used Equation 11
448 to generate 5 random covariance matrices. We constructed a timeseries where each set of 60 consecutive
449 samples was drawn from a Gaussian with the same covariance matrix. These datasets were intended to
450 simulate a system that exhibits periods of stability punctuated by occasional abrupt state changes.

451 **Synthetic data: simulating dynamic high-order correlations**

452 We developed an iterative procedure for constructing timeseries data that exhibits known dynamic high-
453 order correlations. The procedure builds on our approach to generating dynamic first-order correlations.
454 Essentially, once we generate a timeseries with known first-order correlations, we can use the known first-
455 order correlations as a template to generate a new timeseries of second-order correlations. In turn, we can
456 generate a timeseries of third-order correlations from the second-order correlations, and so on. In general,
457 we can generate order n correlations given a timeseries of order $n - 1$ correlations, for any $n > 1$. Finally,
458 given the order n timeseries, we can reverse the preceding process to generate an order $n - 1$ timeseries, an
459 order $n - 2$ order timeseries, and so on, until we obtain an order 0 timeseries of simulated data that reflects
460 the chosen high-order dynamics.

461 The central mathematical operation in our procedure is the Kronecker product (\otimes). The Kronecker
462 product of a $K \times K$ matrix, m_1 , with itself (i.e., $m_1 \otimes m_1$) produces a new $K^2 \times K^2$ matrix, m_2 whose entries reflect
463 a scaled tiling of the entries in m_1 . If these tilings (scaled copies of m_1) are indexed by row and column, then
464 the tile in the i^{th} row and j^{th} column contains the entries of m_1 , multiplied by $m_1(i, j)$. Following this pattern,
465 the Kronecker product $m_2 \otimes m_2$ yields the $K^4 \times K^4$ matrix m_3 whose tiles are scaled copies of m_2 . In general,
466 repeated applications of the Kronecker self-product may be used to generate $m_{n+1} = m_n \otimes m_n$ for $n > 1$, where
467 m_{n+1} is a $K^{2^n} \times K^{2^n}$ matrix. After generating a first-order timeseries of dynamic correlations (see *Synthetic*
468 *data: simulating dynamic first-order correlations* [Synthetic data: simulating dynamic first-order correlations](#)),
469 we use this procedure (applied independently at each timepoint) to transform it into a timeseries of n^{th} -order
470 correlations. When m_{n+1} is generated in this way, the temporal structure of the full timeseries (i.e., constant,
471 random, ramping, event) is preserved, since changes in the original first-order timeseries are also reflected
472 in the scaled tilings of itself that comprise the higher-order matrices.

473 Given a timeseries of n^{th} -order correlations, we then need to work “backwards” in order to generate the
474 order-zero timeseries. If the n^{th} -order correlation matrix at a given timepoint is m_n , then we can generate an
475 order $n - 1$ correlation matrix (for $n > 1$) by taking a draw from $\mathcal{N}(0, m_n)$ and reshaping the resulting vector
476 to have square dimensions. To force the resulting matrix to be symmetric, we remove its lower triangle, and
477 replace the lower triangle with (a reflected version of) its upper triangle. Intuitively, the *resulting* re-shaped
478 matrix will look like a noisy (but symmetric) version of the template matrix, m_{n-1} . (When $n = 1$, no re-
479 shaping is needed; the resulting K -dimensional vector may be used as the observation at the given timepoint.)
480 After independently drawing each timepoint’s order $n - 1$ correlation matrix from that timepoint’s order
481 n correlation matrix, this process can be applied repeatedly until $n = 0$. This results in a K -dimensional
482 timeseries of T observations containing the specified high-order correlations at orders 1 through n . Following

483 our approach to generating synthetic data exhibiting known first-order correlations, we constructed a total
484 of 400 additional multivariate timeseries, collectively reflecting a total of 4 qualitatively different patterns of
485 dynamic correlations (i.e., 100 datasets reflecting each type of dynamic pattern: constant, random, ramping,
486 and event). Each timeseries comprised 10 zero-order features (dimensions) that varied over 300 timepoints.
487 After applying our dynamic correlation estimation procedure, this yielded a 100-dimensional timeseries of
488 first-order features that could then be used to estimate dynamic second-order correlations. (We chose to
489 use $K = 10$ zero-order features for our higher order simulations in order to put the accuracy computations
490 displayed in Figs. 2 and 3 on a roughly even footing.)

491 **Functional neuroimaging data collected during story listening**

492 We examined an fMRI dataset collected by (36) that the authors have made publicly available at arks.princeton.edu/ark:/88435/
493 The dataset comprises neuroimaging data collected as participants listened to an audio recording of a story
494 (intact condition; 36 participants), listened to temporally scrambled recordings of the same story (17 par-
495 ticipants in the paragraph-scrambled condition listened to the paragraphs in a randomized order and 36
496 in the word-scrambled condition listened to the words in a randomized order), or lay resting with their
497 eyes open in the scanner (rest condition; 36 participants). Full neuroimaging details may be found in the
498 original paper for which the data were collected (36). Procedures were approved by the Princeton
499 University Committee on Activities Involving Human Subjects, and by the Western Institutional Review
500 Board (Puyallup, WA). All subjects were native English speakers with normal hearing and provided written
501 informed consent.

502 **Hierarchical topographic factor analysis (HTFA).** Following our prior related work, we used HTFA (11)
503 (11) to derive a compact representation of the neuroimaging data. In brief, this approach approximates the
504 timeseries of voxel activations (44,415 voxels) using a much smaller number of radial basis function (RBF)
505 nodes ~~(in this case, 700 nodes, as determined by an optimization procedure described by 11)~~ (in this case,
506 700 nodes, as determined by an optimization procedure (11)). This provides a convenient representation
507 for examining full-brain network dynamics. All of the analyses we carried out on the neuroimaging dataset
508 were performed in this lower-dimensional space. In other words, each participant's data matrix, X_0 , was
509 a number-of-timepoints by 700 matrix of HTFA-derived factor weights (where the row and column labels
510 were matched across participants). Code for carrying out HTFA on fMRI data may be found as part of the
511 BrainIAK toolbox (88)(88), which may be downloaded at brainiak.org.

512 **Temporal decoding**

513 We sought to identify neural patterns that reflected participants' ongoing cognitive processing of incoming
514 stimulus information. As reviewed by (36), one way of homing in on these stimulus-driven neural patterns is
515 to compare activity patterns across individuals (e.g., using ISFC analyses). In particular, neural patterns will
516 be similar across individuals to the extent that the neural patterns under consideration are stimulus-driven,
517 and to the extent that the corresponding cognitive representations are reflected in similar spatial patterns
518 across people (also see 55)(55). Following this logic, we used an across-participant temporal decoding test
519 developed by (11) to assess the degree to which different neural patterns reflected ongoing stimulus-driven
520 cognitive processing across people (Fig. 10). The approach entails using a subset of the data to train a
521 classifier to decode stimulus timepoints (i.e., moments in the story participants listened to) from neural
522 patterns. We use decoding (forward inference) accuracy on held-out data, from held-out participants, as a
523 proxy for the extent to which the inputted neural patterns reflected stimulus-driven cognitive processing in
524 a similar way across individuals.

525 **Forward inference and decoding accuracy**

526 We used an across-participant correlation-based classifier to decode which stimulus timepoint matched
527 each timepoint's neural pattern (Fig. 10). We first divided the participants into two groups: a template group,
528 $\mathcal{G}_{\text{template}}$ (i.e., training data), and a to-be-decoded group, $\mathcal{G}_{\text{decode}}$ (i.e., test data). We used Equation 7 to
529 compute a DISFC matrix for each group ($\bar{\mathbf{C}}_{\text{template}}$ and $\bar{\mathbf{C}}_{\text{decode}}$, respectively). We then correlated the rows of
530 $\bar{\mathbf{C}}_{\text{template}}$ and $\bar{\mathbf{C}}_{\text{decode}}$ to form a number-of-timepoints by number-of-timepoints decoding matrix, Λ . In this
531 way, the rows of Λ reflected timepoints from the template group, while the columns reflected timepoints
532 from the to-be-decoded group. We used Λ to assign temporal labels to each row $\bar{\mathbf{C}}_{\text{decode}}$ using the row of
533 $\bar{\mathbf{C}}_{\text{template}}$ with which it was most highly correlated. We then repeated this decoding procedure, but using
534 $\mathcal{G}_{\text{decode}}$ as the template group and $\mathcal{G}_{\text{template}}$ as the to-be-decoded group. Given the true timepoint labels
535 (for each group), we defined the decoding accuracy as the average proportion of correctly
536 decoded timepoints, across both groups. We defined the relative decoding accuracy as the difference between the decoding accuracy and chance accuracy (i.e., $\frac{1}{T}$).
537

538 **Feature weighting and testing**

539 We sought to examine which types of neural features (i.e., activations, first-order dynamic correlations, and
540 higher-order dynamic correlations) were informative to the temporal decoders. Using the notation above,
541 these features correspond to $\mathbf{X}_0, \mathbf{X}_1, \mathbf{X}_2, \mathbf{X}_3$, and so on.

542

[Figure 10 about here.]

543 One challenge to fairly evaluating high-order correlations is that if the kernel used in Equation 4 is
 544 wider than a single timepoint, each repeated application of the equation will result in further temporal
 545 blur. Because our primary assessment metric is temporal decoding accuracy, this unfairly biases against
 546 detecting meaningful signal in higher-order correlations (relative to lower-order correlations). We attempted
 547 to mitigate temporal blur in estimating each \mathbf{X}_n by using a Dirac δ function kernel (which places all of its
 548 mass over a single timepoint; Fig. 9b, 10a) to compute each lower-order correlation ($\mathbf{X}_1, \mathbf{X}_2, \dots, \mathbf{X}_{n-1}$). We
 549 then used a new (potentially wider, as described below) kernel to compute \mathbf{X}_n from \mathbf{X}_{n-1} . In this way,
 550 temporal blurring was applied only in the last step of computing \mathbf{X}_n . We note that, because each \mathbf{X}_n is a
 551 low-dimensional representation of the corresponding \mathbf{Y}_n , the higher-order correlations we estimated reflect
 552 true correlations in the data with lower-fidelity than estimates of lower-order correlations. Therefore, even
 553 after correcting for temporal blurring, our approach is still biased against finding meaningful signal in
 554 higher-order correlations.

555 After computing each $\mathbf{X}_1, \mathbf{X}_2, \dots, \mathbf{X}_{n-1}$ for each participant, we divided participants into two equally sized
 556 groups (± 1 for odd numbers of participants): $\mathcal{G}_{\text{train}}$ and $\mathcal{G}_{\text{test}}$. We then further subdivided $\mathcal{G}_{\text{train}}$ into $\mathcal{G}_{\text{train}_1}$
 557 and $\mathcal{G}_{\text{train}_2}$. We then computed Λ (temporal correlation) matrices for each type of neural feature, using $\mathcal{G}_{\text{train}_1}$
 558 and $\mathcal{G}_{\text{train}_2}$. This resulted in $n + 1$ Λ matrices (one for the original timeseries of neural activations, and one
 559 for each of n orders of dynamic correlations). Our objective was to find a set of weights for each of these Λ
 560 matrices such that the weighted average of the $n + 1$ matrices yielded the highest decoding accuracy. We
 561 used quasi-Newton gradient ascent (89)(89), using decoding accuracy (for $\mathcal{G}_{\text{train}_1}$ and $\mathcal{G}_{\text{train}_2}$) as the objective
 562 function to be maximized, to find an optimal set of training data-derived weights, $\phi_{0,1,\dots,n}$, where $\sum_{i=0}^n \phi_i = 1$
 563 and where $\phi_i \geq 0 \forall i \in [0, 1, \dots, n]$.

564 After estimating an optimal set of weights, we computed a new set of $n + 1$ Λ matrices correlating the
 565 DISFC patterns from $\mathcal{G}_{\text{train}}$ and $\mathcal{G}_{\text{test}}$ at each timepoint. We use the resulting decoding accuracy of $\mathcal{G}_{\text{test}}$
 566 timepoints (using the weights in $\phi_{0,1,\dots,n}$ to average the Λ matrices) to estimate how informative the set of
 567 neural features containing up to n^{th} order correlations were.

568 We used a permutation-based procedure to form stable estimates of decoding accuracy for each set of
 569 neural features. In particular, we computed the decoding accuracy for each of 10 random group assignments
 570 of $\mathcal{G}_{\text{train}}$ and $\mathcal{G}_{\text{test}}$. We report the mean accuracy (along with 95% confidence intervals) for each set of neural
 571 features.

572 **Identifying robust decoding results**

573 The temporal decoding procedure we use to estimate which neural features support ongoing cognitive
574 processing is governed by several parameters. In particular, Equation 4 requires defining a kernel function,
575 which can take on different shapes and widths. For a fixed set of neural features, each of these parameters
576 can yield different decoding accuracies. Further, the best decoding accuracy for a given timepoint may
577 be reliably achieved by one set of parameters, whereas the best decoding accuracy for another timepoint
578 might be reliably achieved by a different set of parameters, and the best decoding accuracy across *all* all
579 timepoints might be reliably achieved by still another different set of parameters. Rather than attempting
580 to maximize decoding accuracy, we sought to discover the trends in the data that were robust to classifier
581 parameters choices. Specifically, we sought to characterize how decoding accuracy varied (under different
582 experimental conditions) as a function of which neural features were considered.

583 To identify decoding results that were robust to specific classifier parameter choices, we repeated our
584 decoding analyses after substituting into Equation 4 each of a variety of kernel shapes and widths. We
585 examined Gaussian (Fig. 9c), Laplace (Fig. 9d), and Mexican Hat (Fig. 9e) kernels, each with widths of 5, 10,
586 20, and 50 samples. We then report the average decoding accuracies across all of these parameter choices.
587 This enabled us to (partially) factor out performance characteristics that were parameter-dependent, within
588 the set of parameters we examined.

589 **Reverse inference**

590 The dynamic patterns we examined comprise high-dimensional correlation patterns at each timepoint. To
591 help interpret the resulting patterns in the context of other studies, we created summary maps by computing
592 the across-timepoint average pairwise correlations at each order of analysis (first order, second order, etc.).
593 We selected the 10 strongest (absolute value) correlations at each order. Each correlation is between the
594 dynamic activity patterns (or patterns of dynamic high-order correlations) measured at two RBF nodes
595 (see *Hierarchical Topographic Factor Analysis*Hierarchical Topographic Factor Analysis). Therefore, the 10
596 strongest correlations involved up to 20 RBF nodes. Each RBF defines a spatial function whose activations
597 range from 0 to 1. We constructed a map of RBF components that denoted the endpoints of the 10 strongest
598 correlations (we set each RBF to have a maximum value of 1). We then carried out a meta analysis using
599 Neurosynth (38) to identify the 10 terms most commonly associated with the given map. This resulted
600 in a set of 10 terms associated with the average dynamic correlation patterns at each order.

601 **Data Availability**

602 The authors declare that the data supporting the findings of this study as well as the source data for
603 this paper are available at github.com/ContextLab/timecorr-paper/releases/tag/v0.4 and has been deposited
604 in the Zenodo database under accession code <https://doi.org/10.5281/zenodo.5165253>. The source data
605 underlying Figs. 2-6 and Supplementary Figs. S1-S9 are provided as a Source Data file. Source Data
606 are provided with the manuscript. The raw fMRI data are protected and are not available due to data
607 privacy laws. The processed fMRI dataset collected by (36) has been made publicly available (91) at
608 arks.princeton.edu/ark:/88435/dsp015d86p269k.

609 **Code Availability**

610 All of our analysis code may be downloaded from github.com/ContextLab/timecorr-paper/releases/tag/v0.4.
611 We have also published a companion Python toolbox that may be downloaded from timecorr.readthedocs.io.

612

613 **Acknowledgements**

614 We acknowledge discussions with Luke Chang, Vassiki Chauhan, Hany Farid, Paxton Fitzpatrick, Andrew
615 Heusser, Eshin Jolly, Aaron Lee, Qiang Liu, Matthijs van der Meer, Judith Mildner, Gina Notaro, Stephen
616 Satterthwaite, Emily Whitaker, Weizhen Xie, and Kirsten Ziman. Our work was supported in part by NSF
617 EPSCoR Award Number 1632738 to J.R.M. and by a sub-award of DARPA RAM Cooperative Agreement
618 N66001-14-2-4-032 to J.R.M. The content is solely the responsibility of the authors and does not necessarily
619 represent the official views of our supporting organizations.

620 **Author contributions**

621 Concept: J.R.M. Implementation: T.H.C., L.L.W.O., and J.R.M. Analyses: L.L.W.O. and J.R.M. Writing:
622 L.L.W.O. and J.R.M.

623 **Competing interests**

624 The authors declare no competing interests.

625 References

- 626 Haxby, J. V. *et al.* Distributed and overlapping representations of faces and objects in ventral temporal
627 cortex. *Science* **293**, 2425–2430 (2001).
- 628 Norman, K. A., Polyn, S. M., Detre, G. J. & Haxby, J. V. Beyond mind-reading: multi-voxel pattern analysis
629 of fMRI data. *Trends in Cognitive Sciences* **10**, 424–430 (2006).
- 630 Tong, F. & Pratte, M. S. Decoding patterns of human brain activity. *Annual Review of Psychology* **63**, 483–509
631 (2012).
- 632 Mitchell, T. M. *et al.* Predicting human brain activity associated with the meanings of nouns. *Science* **320**,
633 1191 (2008).
- 634 Kamitani, Y. & Tong, F. Decoding the visual and subjective contents of the human brain. *Nature Neuroscience*
635 **8**, 679–685 (2005).
- 636 Nishimoto, S. *et al.* Reconstructing visual experience from brain activity evoked by natural movies. *Current
637 Biology* **21**, 1–6 (2011).
- 638 Pereira, F. *et al.* Toward a universal decoder of linguistic meaning from brain activation. *Nature Communications*
639 **9**, 1–13 (2018).
- 640 Huth, A. G., Nisimoto, S., Vu, A. T. & Gallant, J. L. A continuous semantic space describes the representation
641 of thousands of object and action categories across the human brain. *Neuron* **76**, 1210–1224 (2012).
- 642 Huth, A. G., de Heer, W. A., Griffiths, T. L., Theunissen, F. E. & Gallant, J. L. Natural speech reveals the
643 semantic maps that tile human cerebral cortex. *Nature* **532**, 453–458 (2016).
- 644 Etzel, J. A., Gazzola, V. & Keysers, C. An introduction to anatomical ROI-based fMRI classification. *Brain
645 Research* **1281**, 114–125 (2009).
- 646 Manning, J. R. *et al.* A probabilistic approach to discovering dynamic full-brain functional connectivity
647 patterns. *NeuroImage* **180**, 243–252 (2018).
- 648 Fong, A. H. C. *et al.* Dynamic functional connectivity during task performance and rest predicts individual
649 differences in attention across studies. *NeuroImage* **188**, 14–25 (2019).
- 650 Grossberg, S. Nonlinear neural networks: principles, mechanisms, and architectures. *Neural Networks* **1**,
651 17–61 (1988).

- 652 Friston, K. J. The labile brain. I. neuronal transients and nonlinear coupling. *Philosophical Transactions of*
653 *the Royal Society of London* **355B**, 215–236 (2000).
- 654 Sporns, O. & Honey, C. J. Small worlds inside big brains. *Proceedings of the National Academy of Sciences,*
655 *USA* **103**, 19219–19220 (2006).
- 656 Bassett, D., Meyer-Lindenberg, A., Achard, S., Duke, T. & Bullmore, E. Adaptive reconfiguration of fractal
657 small-world human brain functional networks. *Proceedings of the National Academy of Sciences, USA* **103**,
658 19518–19523 (2006).
- 659 Turk-Browne, N. B. Functional interactions as big data in the human brain. *Science* **342**, 580–584 (2013).
- 660 Demertzi, A. *et al.* Human consciousness is supported by dynamic complex patterns of brain signal
661 coordination. *Science Advances* **5**, eaat7603 (2019).
- 662 Solomon, S. H., Medaglia, J. D. & Thompson-Schill, S. L. Implementing a concept network model. *Behavior*
663 *Research Methods* **51**, 1717–1736 (2019).
- 664 Lurie, D. *et al.* On the nature of time-varying functional connectivity in resting fMRI. *PsyArXiv*
665 doi.org/10.31234/osf.io/xtzre (2018).
- 666 Preti, M. G., Bolton, T. A. W. & Van De Ville, D. The dynamic functional connectome: state-of-the-art and
667 perspectives. *NeuroImage* **160**, 41–54 (2017).
- 668 Zou, Y., Donner, R. V., Marwan, N., Donges, J. F. & Kurths, J. Complex network approaches to nonlinear
669 time series analysis. *Physics Reports* **787**, 1–97 (2019).
- 670 Mack, M. L., Preston, A. R. & Love, B. C. Medial prefrontal cortex compresses concept representations
671 through learning. *bioRxiv* doi.org/10.1101/178145 (2017).
- 672 Bressler, S. L. & Kelso, J. A. S. Cortical coordination dynamics and cognition. *Trends in Cognitive Sciences* **5**,
673 26–36 (2001).
- 674 McIntosh, A. R. Towards a network theory of cognition. *Neural Networks* **13**, 861–870 (2000).
- 675 Reimann, M. W. *et al.* Cliques of neurons bound into cavities provide a missing link between structure and
676 function. *Frontiers in Computational Neuroscience* **11**, 1–16 (2017).
- 677 Beaty, R. E., Benedek, M., Silvia, P. J. & Schacter, D. L. Creative cognition and brain network dynamics.
678 *Trends in Cognitive Sciences* **20**, 87–95 (2016).

- 679 Bullmore, E. & Sporns, O. Complex brain networks: graph theoretical analysis of structural and functional
680 systems. *Nature Reviews Neuroscience* **10**, 186–198 (2009).
- 681 Pearson, K. On lines and planes of closest fit to systems of points in space. *The London, Edinburgh, and*
682 *Dublin Philosophical Magazine and Journal of Science* **2**, 559–572 (1901).
- 683 McIntosh, A. R. & Jirsa, V. K. The hidden repertoire of brain dynamics and dysfunction. *Network Neuroscience*
684 doi.org/10.1162/netn_a.00107 (2019).
- 685 Toker, D. & Sommer, F. T. Information integration in large brain networks. *PLoS Computational Biology* **15**,
686 e1006807 (2019).
- 687 Gonzalez-Castillo, J. *et al.* Imaging the spontaneous flow of thought: distinct periods of cognition contribute
688 to dynamic functional connectivity during rest. *NeuroImage* **202** (2019).
- 689 Landau, E. Zur relativen Wertbemessung der Turnierresultate. *Deutsches Wochenschach* **11**, 366–369 (1895).
- 690 Betzel, R. F., Byrge, L., Esfahlani, F. Z. & Kennedy, D. P. Temporal fluctuations in the brain's modular
691 architecture during movie-watching. *bioRxiv* doi.org/10.1101/750919 (2019).
- 692 Sizemore, A. E. *et al.* Cliques and cavities in the human connectome. *Journal of Computational Neuroscience*
693 **44**, 115–145 (2018).
- 694 Simony, E., Honey, C. J., Chen, J. & Hasson, U. Dynamic reconfiguration of the default mode network
695 during narrative comprehension. *Nature Communications* **7**, 1–13 (2016).
- 696 Hasson, U., Yang, E., Vallines, I., Heeger, D. J. & Rubin, N. A hierarchy of temporal receptive windows in
697 human cortex. *The Journal of Neuroscience* **28**, 2539–2550 (2008).
- 698 Rubin, T. N. *et al.* Decoding brain activity using a large-scale probabilistic functional-anatomical atlas of
699 human cognition. *PLoS Computational Biology* **13**, e1005649 (2017).
- 700 Park, H.-J., Friston, K. J., Pae, C., Park, B. & Razi, A. Dynamic effective connectivity in resting state fMRI.
701 *NeuroImage* **180**, 594–608 (2018).
- 702 Roy, D. S. *et al.* Brain-wide mapping of contextual fear memory engram ensembles supports the dispersed
703 engram complex hypothesis. *bioRxiv* doi.org/10.1101/668483 (2019).
- 704 Liégeois, R. *et al.* Resting brain dynamics at different timescales capture distinct aspects of human behavior.
705 *Nature Communications* **10**, 1–9 (2019).

- 706 Chang, C. & Glover, G. H. Time-frequency dynamics of resting-state brain connectivity measured with
707 fMRI. *NeuroImage* **50**, 81–98 (2010).
- 708 Zheng, M., Allard, A., Hagmann, P. & Serrano, M. . . A. Geometric renormalization unravels self-similarity
709 of the multiscale human connectome. *arXiv* **1904.11793** (2019).
- 710 Baldassano, C. *et al.* Discovering event structure in continuous narrative perception and memory. *Neuron*
711 **95**, 709–721 (2017).
- 712 Hasson, U., Chen, J. & Honey, C. J. Hierarchical process memory: memory as an integral component of
713 information processing. *Trends in Cognitive Sciences* **19**, 304–315 (2015).
- 714 Honey, C. J. *et al.* Slow cortical dynamics and the accumulation of information over long timescales. *Neuron*
715 **76**, 423–434 (2012).
- 716 Lerner, Y., Honey, C. J., Silbert, L. J. & Hasson, U. Topographic mapping of a hierarchy of temporal receptive
717 windows using a narrated story. *The Journal of Neuroscience* **31**, 2906–2915 (2011).
- 718 Lerner, Y., Honey, C. J., Katkov, M. & Hasson, U. Temporal scaling of neural responses to compressed and
719 dilated natural speech. *Journal of Neurophysiology* **111**, 2433–2444 (2014).
- 720 Chien, H.-Y. S. & Honey, C. J. Constructing and forgetting temporal context in the human cerebral cortex.
721 *bioRxiv* doi.org/10.1101/761593 (2019).
- 722 Lee, C. S., Aly, M. & Baldassano, C. Anticipation of temporally structured events in the brain. *bioRxiv*
723 **10.1101/2020.10.14.338145** (2020).
- 724 Fallon, J., Ward, P. G. D., Parkes, L. & Oldham, S. Timescales of spontaneous fMRI fluctuations relate to
725 structural connectivity in the brain. *Network Neuroscience* **4**, 788–806 (2020).
- 726 Shappell, H., Caffo, B. S., Pekar, J. J. & Lindquist, M. A. Improved state change estimation in dynamic
727 functional connectivity using hidden semi-Markov models. *NeuroImage* **191**, 243–257 (2019).
- 728 Vidaurre, D. *et al.* Discovering dynamic brain networks from big data in rest and task. *NeuroImage* **180**,
729 646–656 (2018).
- 730 Allen, E. A. *et al.* Tracking whole-brain connectivity dynamics in the resting state. *Cerebral Cortex* **24**,
731 663–676 (2012).
- 732 Simony, E. & Chang, C. Analysis of stimulus-induced brain dynamics during naturalistic paradigms.
733 *NeuroImage* **216**, 116461 (2020).

- 734 Zar, J. H. *Biostatistical analysis* (Prentice-Hall, 2010).
- 735 Tipping, M. E. & Bishop, C. M. Probabilistic principal component analysis. *Journal of Royal Statistical Society, Series B* **61**, 611–622 (1999).
- 736 Spearman, C. General intelligence, objectively determined and measured. *American Journal of Psychology* **15**, 201–292 (1904).
- 737 Jutten, C. & Herault, J. Blind separation of sources, part I: an adaptive algorithm based on neuromimetic architecture. *Signal Processing* **24**, 1–10 (1991).
- 738 Comon, P., Jutten, C. & Herault, J. Blind separation of sources, part II: problems statement. *Signal Processing* **24**, 11–20 (1991).
- 739 van der Maaten, L. J. P. & Hinton, G. E. Visualizing high-dimensional data using t-SNE. *Journal of Machine Learning Research* **9**, 2579–2605 (2008).
- 740 McInnes, L., Healy, J. & Melville, J. UMAP: uniform manifold approximation and projection for dimension reduction. *arXiv* **1802** (2018).
- 741 Lee, D. D. & Seung, H. S. Learning the parts of objects by non-negative matrix factorization. *Nature* **401**, 788–791 (1999).
- 742 Manning, J. R., Ranganath, R., Norman, K. A. & Blei, D. M. Topographic factor analysis: a Bayesian model for inferring brain networks from neural data. *PLoS One* **9**, e94914 (2014).
- 743 Gershman, S. J., Blei, D. M., Pereira, F. & Norman, K. A. A topographic latent source model for fMRI data. *NeuroImage* **57**, 89–100 (2011).
- 744 Mairal, J., Bach, F., Ponce, J. & Sapiro, G. Online dictionary learning for sparse coding. *Proceedings of the International Conference on Machine Learning* 689–696 (2009).
- 745 Mairal, J., Ponce, J., Sapiro, G., Zisserman, A. & Bach, F. R. Supervised dictionary learning. *Advances in Neural Information Processing Systems* 1033–1040 (2009).
- 746 Hinton, G. E. & Salakhutdinov, R. R. Reducing the dimensionality of data with neural networks. *Science* **313**, 504–507 (2006).
- 747 Newman, M. E. J. A measure of betweenness centrality based on random walks. *Social Networks* **27**, 39–54 (2005).

- 761 Opsahl, T., Agneessens, F. & Skvoretz, J. Node centrality in weighted networks: generalizing degree and
762 shortest paths. *Social Networks* **32**, 245–251 (2010).
- 763 Barthélémy, M. Betweenness centrality in large complex networks. *European Physical Journal B* **38**, 163–168
764 (2004).
- 765 Geisberger, R., Sanders, P. & Schultes, D. Better approximation of betweenness centrality. *Proceedings of
766 the Meeting on Algorithm Engineering and Experiments* 90–100 (2008).
- 767 Freeman, L. C. A set of measures of centrality based on betweenness. *Sociometry* **40**, 35–41 (1977).
- 768 Rao, C. R. Diversity and dissimilarity coefficients: a unified approach. *Theoretical Population Biology* **21**,
769 24–43 (1982).
- 770 Lin, J. Divergence measures based on the Shannon entropy. *IEEE Transactions on Information Theory* **37**,
771 145–151 (2009).
- 772 Ricotta, C. & Szeidl, L. Towards a unifying approach to diversity measures: bridging the gap between the
773 Shannon entropy and Rao's quadratic index. *Theoretical Population Biology* **70**, 237–243 (2006).
- 774 Newman, M. E. J. The mathematics of networks. *The New Palgrave Encyclopedia of Economics* **2**, 1–12 (2008).
- 775 Bonacich, P. Some unique properties of eigenvector centrality. *Social Networks* **29**, 555–564 (2007).
- 776 Lohmann, G. *et al.* Eigenvector centrality mapping for analyzing connectivity patterns in fMRI data of the
777 human brain. *PLoS One* **5**, e10232 (2010).
- 778 Halu, A., Mondragón, R. J., Panzarasa, P. & Bianconi, G. Multiplex PageRank. *PLoS One* **8**, e78293 (2013).
- 779 Honey, C. J., Kötter, R., Breakspear, M. & Sporns, O. Network structure of cerebral cortex shapes functional
780 connectivity on multiple time scales. *Proceedings of the National Academy of Sciences, USA* **104**, 10240–10245
781 (2007).
- 782 Schreiber, T. Measuring information transfer. *Physical Review Letters* **85**, 461–464 (2000).
- 783 Alvarez-Hamelin, I., Dall'Asta, L., Barrat, A. & Vespignani, A. k-corr decomposition: a tool for the
784 visualization of large scale networks. *arXiv cs/0504107v2* (2005).
- 785 Christakis, N. A. & Fowler, J. H. Social network sensors for early detection of contagious outbreaks. *PLoS
786 One* **5**, e12948 (2010).

- 787 Rubinov, M. & Sporns, O. Complex network measures of brain connectivity: uses and interpretations.
788 *NeuroImage* **52**, 1059–1069 (2010).
- 789 Estrada, E. & Rodríguez-Velázquez, J. A. Subgraph centrality in complex networks. *Physical Review E* **71**,
790 056103 (2005).
- 791 Thompson, W. H., Richter, C. G., Plavén-Sigray, P. & Fransson, P. Simulations to benchmark time-varying
792 connectivity methods for fMRI. *PLoS Computational Biology* **14**, e1006196 (2018).
- 793 Capota, M. *et al.* Brain imaging analysis kit (2017).
- 794 Nocedal, J. & Wright, S. J. *Numerical optimization* (Springer, New York, NY, 2006).
- 795 Combrisson, E. *et al.* Visbrain: a multi-purpose GPU-accelerated open-source suite for multimodal brain
796 data visualization. *Frontiers in Neuroinformatics* **13**, 1–14 (2019).
- 797 Simony, E., Honey, C. J., Chen, J. & Hasson, U. Dynamic reconfiguration of the default mode network
798 during narrative comprehension. *DataSpace* <http://arks.princeton.edu/ark:/88435/dsp015d86p269k> (2016).

800 **Figures**

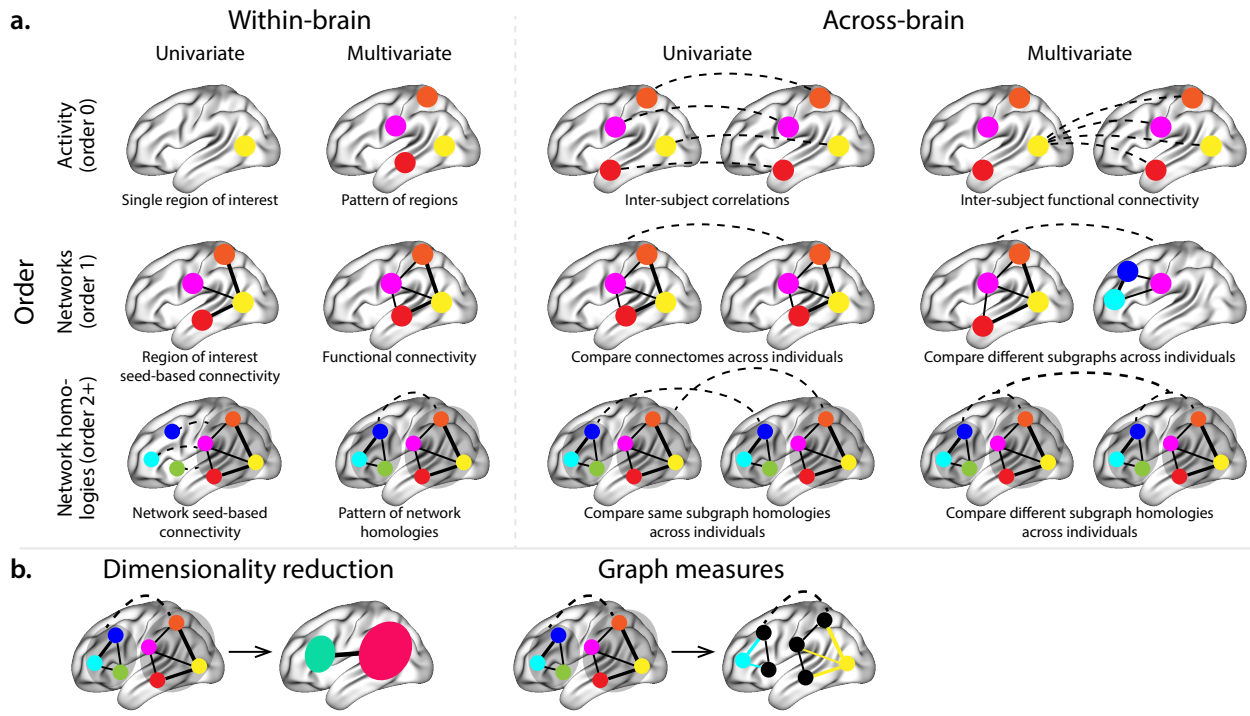


Figure 1: Neural patterns. a. A space of neural features. Within-brain analyses are carried out within a single brain, whereas across-brain analyses compare neural patterns across two or more individuals' brains. Univariate analyses characterize the activities of individual units (e.g., nodes, small networks, hierarchies of networks, etc.), whereas multivariate analyses characterize the patterns of activity across units. Order 0 patterns involve individual nodes; order 1 patterns involve node-node interactions; order 2 (and higher) patterns relate to interactions between homologous networks. Each of these patterns may be static (e.g., averaging over time) or dynamic. **b. Summarizing neural patterns.** To efficiently compute with complex neural patterns, it can be useful to characterize the patterns using summary measures. Dimensionality reduction algorithms project the patterns onto lower-dimensional spaces whose dimensions reflect weighted combinations or non-linear transformations of the dimensions in the original space. Graph measures characterize each unit's participation in its associated network.

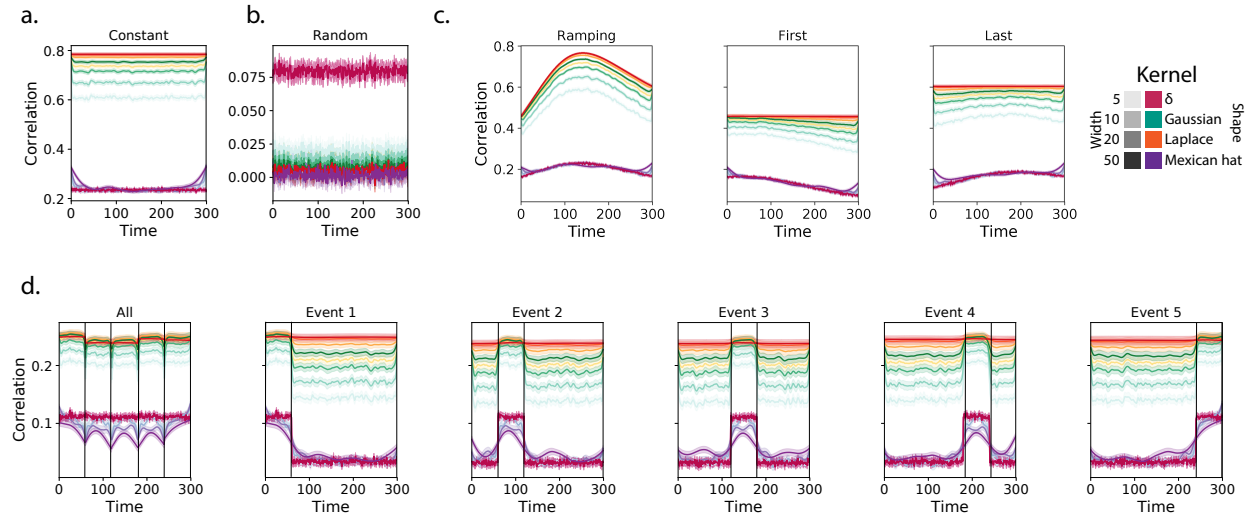


Figure 2: Recovering known dynamic first-order correlations from synthetic data. Each panel displays the average correlations between the vectorized upper triangles of the recovered correlation matrix at each timepoint and either the true underlying correlation at each timepoint or a reference correlation matrix. (The averages are taken across 100 different randomly generated synthetic datasets of each given category, each with $K = 50$ features and $T = 300$ timepoints.) Error ribbons denote 95% confidence intervals [of the mean](#) (taken across datasets). Different colors denote different kernel shapes, and the shading within each color family denotes the kernel width parameter. For a complete description of each synthetic dataset, see [Synthetic data: simulating dynamic first-order correlations](#) [Synthetic data: simulating dynamic first-order correlations](#).

a. Constant correlations. These datasets have a stable (unchanging) underlying correlation matrix.

b. Random correlations. These datasets are generated using a new independently drawn correlation matrix at each new timepoint.

c. Ramping correlations. These datasets are generated by smoothly varying the underlying correlations between the randomly drawn correlation matrices at the first and last timepoints. The left panel displays the correlations between the recovered dynamic correlations and the underlying ground truth correlations. The middle panel compares the recovered correlations with the [first](#) [first](#) timepoint's correlation matrix. The right panel compares the recovered correlations with the [last](#) [last](#) timepoint's correlation matrix.

d. Event-based correlations. These datasets are each generated using five randomly drawn correlation matrices that each remain stable for a fifth of the total timecourse. The left panel displays the correlations between the recovered dynamic correlations and the underlying ground truth correlations. The right panels compare the recovered correlations with the correlation matrices unique to each event. The vertical lines denote event boundaries. [Source data are provided as a Source Data file](#).

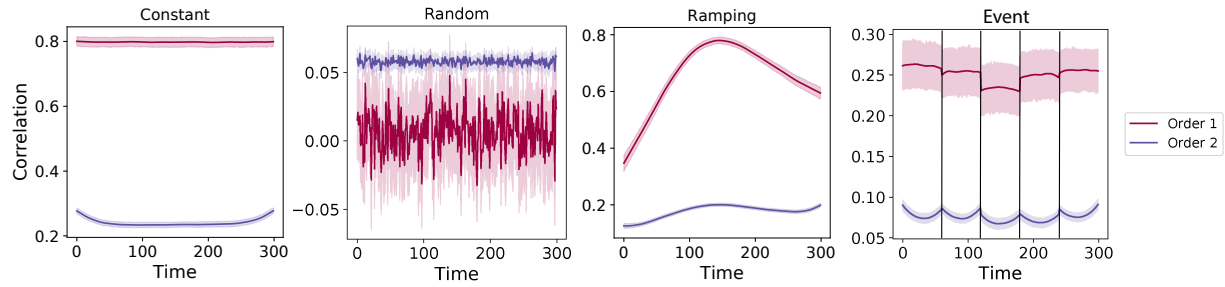


Figure 3: Recovery of simulated first-order and second-order dynamic correlations. Each panel displays the average correlations between the vectorized upper triangles of the recovered first-order and second-order correlation matrices and the true (simulated) first-order and second order correlation matrices at each timepoint and for each synthetic dataset. (The averages are taken across 100 different randomly generated synthetic datasets of each given category, each with $K = 10$ features and $T = 300$ timepoints.) Error ribbons denote 95% confidence intervals of the mean (taken across datasets). For a complete description of each synthetic dataset, see [Synthetic data: simulating dynamic higher-order correlations](#). All estimates represented in this figure were computed using a Laplace kernel (width = 20). **Constant.** These datasets have stable (unchanging) underlying second-order correlation matrices. **Random.** These datasets are generated using a new independently drawn second-order correlation matrix at each timepoint. **Ramping.** These datasets are generated by smoothly varying the underlying second-order correlations between the randomly drawn correlation matrices at the first and last timepoints. **Event.** These datasets are each generated using five randomly drawn second-order correlation matrices that each remain stable for a fifth of the total timecourse. The vertical lines denote event boundaries. Note that the “dips” and “ramps” at the boundaries of sharp transitions (e.g., the beginning and ends of the “constant” and “ramping” datasets, and at the event boundaries of the “event” datasets) are finite-sample effects that reflect the reduced numbers of samples that may be used to accurately estimate correlations at sharp boundaries. [Source data are provided as a Source Data file](#).

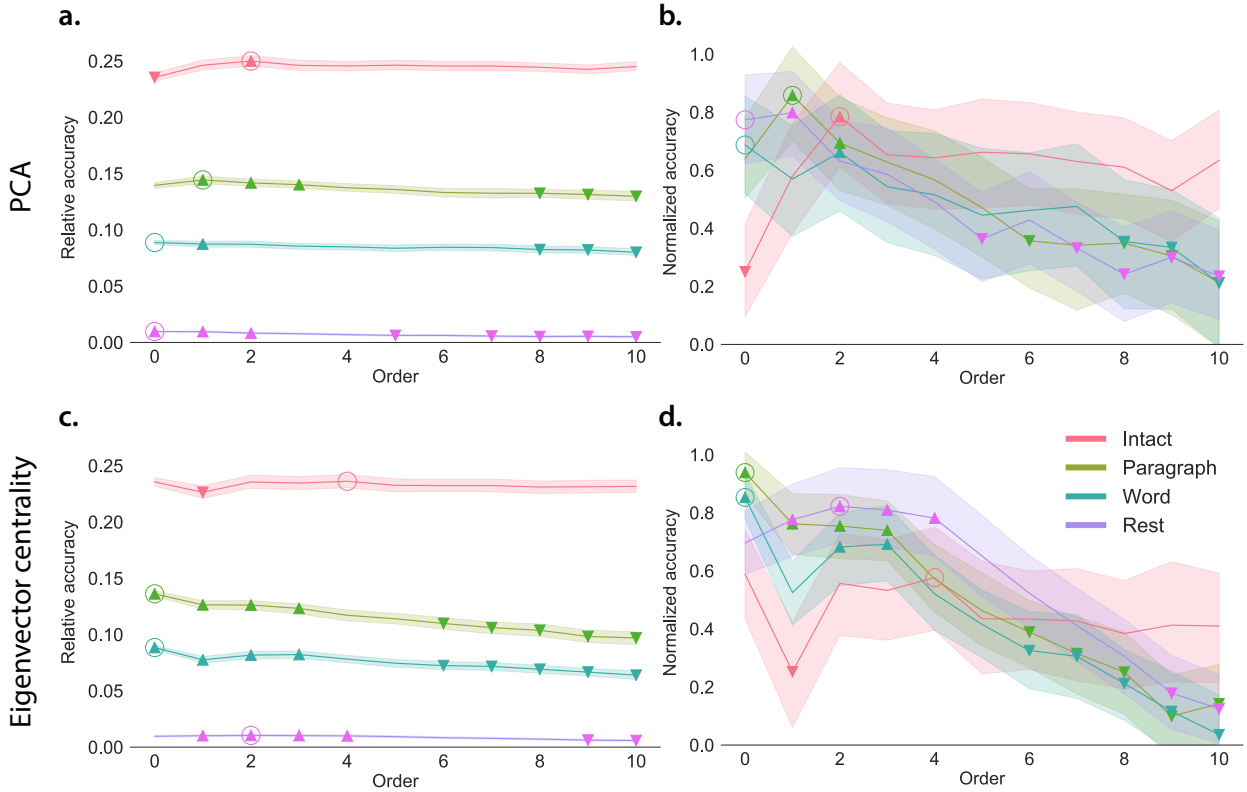


Figure 4: Across-participant timepoint decoding accuracy varies with correlation order and cognitive engagement.

a. Decoding accuracy as a function of order: PCA. Order “Order” (x-axis) refers to the maximum order of dynamic correlations that were available to the classifiers (see [Feature weighting and testing](#)). The reported across-participant decoding accuracies are averaged over all kernel shapes and widths (see [Identifying robust decoding results](#)). The y-values are displayed relative to chance accuracy (intact: $\frac{1}{300}$; paragraph: $\frac{1}{272}$; word: $\frac{1}{300}$; rest: $\frac{1}{400}$; these chance accuracies were subtracted from the observed accuracies to obtain the relative accuracies reported on the y-axis). The error ribbons denote 95% confidence intervals of the means across cross-validation folds (i.e., random assignments of participants to the training and test sets). The colors denote the experimental condition. Arrows denote sets of features that yielded reliably higher (upward facing) or lower (downward facing) decoding accuracy than the mean of all other features (via a two-tailed t -test, thresholded at $p < 0.05$). Figure 5 displays additional comparisons between the decoding accuracies achieved using different sets of neural features. The circled values represent the maximum decoding accuracy within each experimental condition.

b. Normalized timepoint decoding accuracy as a function of order: PCA. This panel displays the same results as Panel a, but here each curve has been normalized to be bounded between 0 and have a maximum value of 1 (inclusive) by subtracting the minimum accuracy value of 0 (across all folds and orders) and then dividing by including the maximum accuracy (again, across all folds upper and orders lower bounds of the respective 95% confidence intervals of the mean).

c. Timepoint decoding accuracy as a function of order: eigenvector centrality. This panel is in the same format as Panel a, but here eigenvector centrality has been used to project the high-dimensional patterns of dynamic correlations onto a lower-dimensional space.

d. Normalized timepoint decoding accuracy as a function of order: eigenvector centrality. This panel is in the same format as Panel b, but here eigenvector centrality has been used to project the high-dimensional patterns of dynamic correlations onto a lower-dimensional space. See Figures S1 and S2 for decoding results broken down by kernel shape and width, respectively. [Source data are provided as a Source Data file](#).

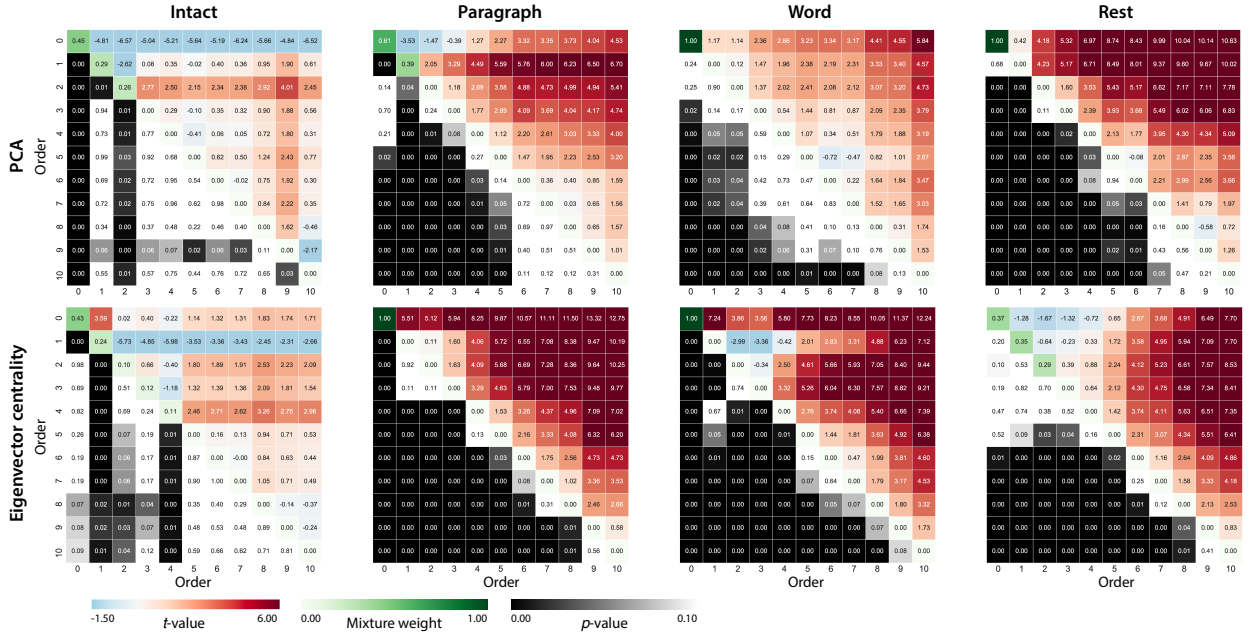


Figure 5: Statistical summary of decoding accuracies for different neural features. Each column of matrices displays decoding results for one experimental condition (intact, paragraph, word, and rest). We considered dynamic activity patterns (order 0) and dynamic correlations at different orders (order > 0). We used two-tailed t -tests to compare the distributions of decoding accuracies obtained using each pair of features. The distributions for each feature reflect the set of average decoding accuracies (across all kernel parameters), obtained for each random assignment of training and test groups. In the upper triangles of each matrix, warmer colors (positive t -values) indicate that the neural feature indicated in the given row yielded higher accuracy than the feature indicated in the given column. Cooler colors (negative t -values) indicate that the feature in the given row yielded lower decoding accuracy than the feature in the given column. The lower triangles of each map denote the corresponding p -values for the t -tests. The diagonal entries display the relative average optimized weight given to each type of feature in a decoder that included all feature types (see [Feature weighting and testing](#)).

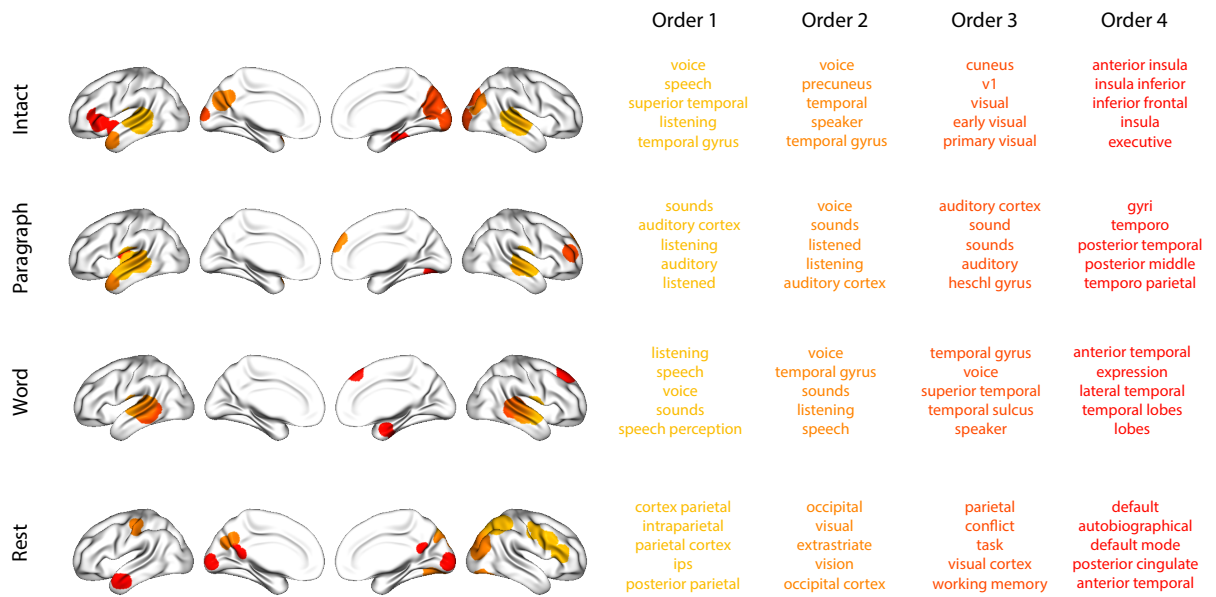


Figure 6: Top terms associated with the most strongly correlated nodes at each order. Each color corresponds to one order of inter-subject functional correlations. To calculate the dynamic correlations, eigenvector centrality has been used to project the high-dimensional patterns of dynamic correlations onto a lower-dimensional space at each previous order, which allows us to map the brain regions at each order by retaining the features of the original space. The inflated brain plots display the locations of the endpoints of the 10 strongest (absolute value) correlations at each order, thresholded at 0.999, and projected onto the cortical surface (90)(90). The lists of terms on the right display the top five Neurosynth terms (38)(38) decoded from the corresponding brain maps for each order. Each row displays data from a different experimental condition. Additional maps and their corresponding Neurosynth terms may be found in the [Supplementary materials](#) (intact: Fig. S5; paragraph: Fig. S6; word: Fig. S7; rest: Fig. S8). [Source data are provided as a Source Data file](#).

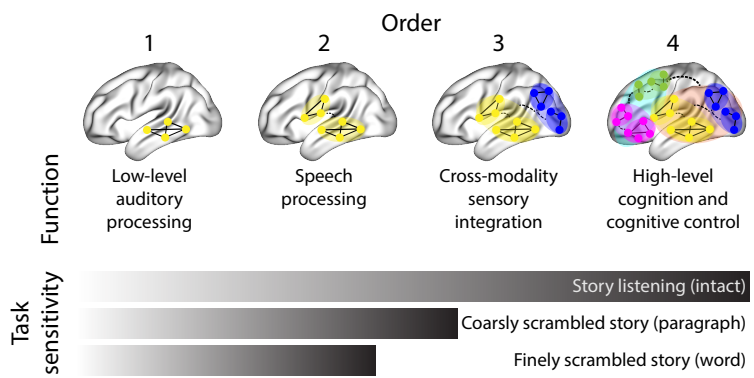


Figure 7: Proposed high-order network dynamics underlying high-level cognition during story listening. Schematic depicts higher orders of network interactions supporting higher-level aspects of cognitive processing. When tasks evoke richer, deeper, and/or higher-level processing, this is reflected in higher-order network interactions.

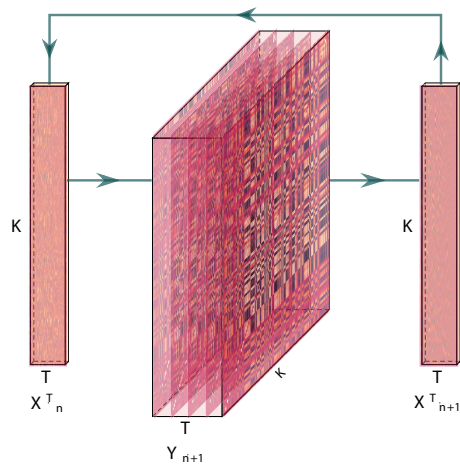


Figure 8: Estimating dynamic high-order correlations. Given a T by K matrix of multivariate timeseries data, \mathbf{X}_n (where $n \in \mathbb{N}, n \geq 0$), we use Equation 4 to compute a timeseries of K by K correlation matrices, \mathbf{Y}_{n+1} . We then approximate \mathbf{Y}_{n+1} with the T by K matrix \mathbf{X}_{n+1} . This process may be repeated to scalably estimate iteratively higher-order correlations in the data. Note that the transposes of \mathbf{X}_n and \mathbf{X}_{n+1} are displayed in the figure for compactness.

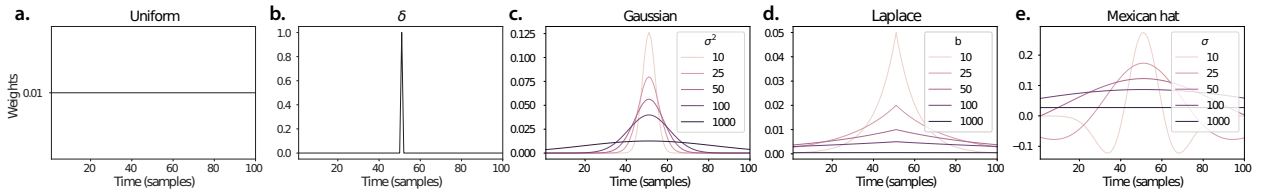


Figure 9: Examples of kernel functions. Each panel displays per-timepoint weights for a kernel centered at $t = 50$, evaluated at 100 timepoints ($\tau \in [1, \dots, 100]$). **a. Uniform kernel.** The weights are timepoint-invariant; observations at all timepoints are weighted equally, and do not change as a function of τ . This is a special case kernel function that reduces dynamic correlations to static correlations. **b. Dirac δ kernel.** Only the observation at timepoint t is given a non-zero weight (of 1). **c. Gaussian kernels.** Each kernel's weights fall off in time according to a Gaussian probability density function centered on time t . Weights derived using several different example width parameters (σ^2) are displayed. **d. Laplace kernels.** Each kernel's weights fall off in time according to a Laplace probability density function centered on time t . Weights derived using several different example width parameters (b) are displayed. **e. Mexican hat (Ricker wavelet) kernels.** Each kernel's weights fall off in time according to a Ricker wavelet centered on time t . This function highlights the contrasts between local versus surrounding activity patterns in estimating dynamic correlations. Weights derived using several different example width parameters (σ) are displayed.

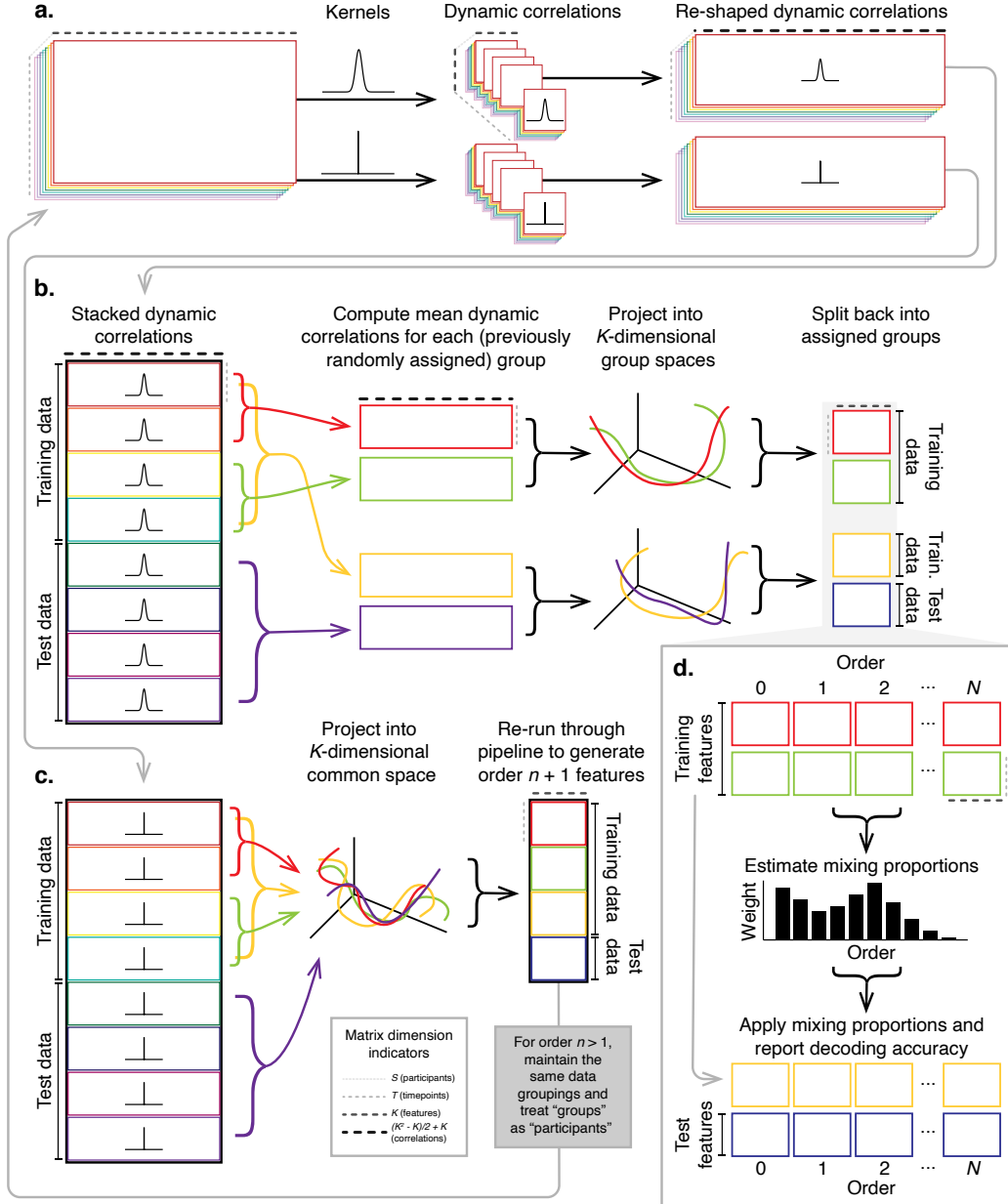


Figure 10: Decoding analysis pipeline. **a. Computing dynamic correlations from timeseries data.** Given a timeseries of observations as a $T \times K$ matrix (or a set of S such matrices), we use Equation 4 to compute each participant's DISFC (relative to other participants in the training or test sub-group, as appropriate). We repeat this process twice—once using the analysis kernel (shown here as a Gaussian in the upper row of the panel), and once using a δ function kernel (lower row of the panel). **b. Projecting dynamic correlations into a lower-dimensional space.** We project the training and test data into K -dimensional spaces to create compact representations of dynamic correlations at the given order (estimated using the analysis kernel). **c. Kernel trick.** We project the dynamic correlations computed using a δ function kernel into a common K -dimensional space. These low-dimensional embeddings are fed back through the analysis pipeline in order to compute features at the next-highest order. **d. Decoding analysis.** We split the training data into two equal groups, and optimize the feature weights (i.e., dynamic correlations at each order) to maximize decoding accuracy. We then apply the trained classifier to the (held-out) test data.